2016

A Numerical Investigation of Wellbore Stability Problems Using an Elastoplastic Model

Chang Huang
Louisiana State University and Agricultural and Mechanical College, huangchang73@gmail.com

A NUMERICAL INVESTIGATION OF WELLBORE STABILITY PROBLEMS USING AN ELASTOPLASTIC MODEL

A Thesis

Submitted to the Graduate Faculty of the
Louisiana State University and
Agricultural and Mechanical College
in partial fulfillment of the
requirements for the degree of
Master of Science in Petroleum Engineering

in

The Department of Petroleum Engineering

by
Chang Huang
B.E., China University of Petroleum, China, 2014
August 2016

Acknowledgments

My thanks are due to Dr. Babak Akbari and Dr. Shengli Chen for their guidance and support through the research project. I wouldn't have finished my thesis without their help.

In particular, I thank Dr. Andrew Wojtanowicz for sharing his wealth of experience and knowledge during my study at Louisiana State University. I would also like to thank Dr. Mayank Tyagi for his involvement in the committee for the thesis. I would like to thank Dr. Arash Dahi for his good explanation of tensor algebra within the reservoir geomechanics course.

Also, I want to show my gratitude to Dr. Nicola Castelletto and Dr. Yashar Mehmani in Stanford University for their help in guiding me to the right direction in the early stage.

Special thanks go to American Association of Drilling Engineers—New Orleans Chapter for their financial support in the past one year.

Thanks also to my fellow students and my good friend Mohammad Munawar, Christian Griman, and Hong Yao for their help in general. Finally, I want to thank my family for supporting me all the time!

Table of Contents

Abstract

Wellbore stability analysis acts an important role in the drilling design to avoid stuck-pipe, lost circulation and the other instability-induced problems. However, the conventional linear elastic model used by the industry is too conservative in predicting the mud weight window. This project is aimed at improving the accuracy of wellbore stability analysis. An elastoplastic model with Drucker-Prager yield criterion featured by strain hardening is proposed to characterize the rock behavior. Object-oriented finite element analysis simulator, NSMOOM, is programmed in MATLAB. The simulator is verified with the analytical solution in the elastic domain and with the commercial software ABAQUS in the elastoplastic domain. Upon the good verification results, the code is applied to an under-balanced-drilling case. For the case study, a good match is shown between the prediction of the proposed elastoplastic model and the actual wellbore response. On the other hand, no available mud weight window for under-balanced-drilling can be calculated by the pure elastic model. In conclusion, the proposed model provides a more realistic tool to predict wellbore stability.

Chapter 1 Introduction

The major part of the investment to construct a well is to deal with wellbore-instability-induced problems, like wellbore collapse, stuck pipe, and lost circulation, etc. According to a survey conducted by SPEreview in 2005, wellbore instability problems cost more than 6 billion US dollars worldwide annually (Kang, Yu, Miska, & Takach, 2009). Along with the increasing number of deviated wells, or wells encountering high-pressure and high-temperature conditions, the demand for wellbore stability maintenance technique is increasing accordingly. The maintenance technique has many steps to go through the drilling process. The most important and the most studied step is wellbore stability analysis, by which the adjustment of wellbore path, casing profile and mud weight and mud type are determined.

The conventional linear elastic model is usually very conservative in predicting the mud weight window. As a result, many well designs have to increase the casing sections which turns out to be unnecessary. In other cases, the traditional design ends up with unavailable mud window. In fact, rock property is never nearly as simple as the linear elastic model predicts. The nonlinear plastic behavior of rocks has been studied by many researchers. It has been commonly accepted that a plastic model is a technique to better represent the rock behavior. This project is designed to provide a numerical technique to guide the wellbore stability analysis in the drilling industry with a more realistic strain hardening elastoplastic model. The study is aimed at investigating the failure mechanism by observing the extension of the plastic zone in the near wellbore region rather than focusing on the boundary only.

1.1 Overview of each chapter

In Chapter 2, the major work in the application of elastoplastic model to the wellbore stability analysis is reviewed first followed by the criterion to determine the wellbore failure. Strain

hardening Drucker-Prager model is selected. In addition, the programming approaches of the finite element solution for the elastoplastic analysis are discussed. Object-oriented programming is chosen because of its suitability in programming a modular algorithm.

The problem is defined in Chapter 3. It is abstracted from real wellbore drilling scenarios by introducing several assumptions. Chapter 4 elaborates the methods used to solve the problem. The general elastoplastic theory is briefly explained first. Then Drucker-Prager model is formulated in the fashion of the general elastoplastic model. In the following, the nonlinear finite element method used is explained in detail. At last, the finite element formulation of Drucker-Prager model is derived which can be used as pseudocode for the actual program, NSMOOM.

Chapter 5 overviews the structure of the NSMOOM by explaining the fundamentals of object-oriented programming first. With the terminology, the structure of the program is showed in a class diagram. Finally, the flowchart of the main algorithm in the simulator is explained.

The verification is carried out in Chapter 6 and Chapter 7 with focus on the elastic domain and the elastoplastic domain respectively. Within elastic domain, the program is verified with the analytical solution. The comparison shows good match between the code and the analytical solution. Then the developed code is compared to a commercial software ABAQUS in the whole elastoplastic domain. Good match is observed in various comparisons.

Chapter 7 studies the wellbore deformation from multiple aspects. The evolution of the yielded zone in the near wellbore region during the incremental loading is analyzed. A prediction of wellbore stability is given based on the normalized yielded zone area. The analysis is discussed and compared to other simulations.

The conclusions, discussions and recommendations are summarized in Chapter 8.

1.2 Conventions and important characters

The sign convention in this thesis defines tensile stress and strain as positive. Thus compressive stress and strain are negative.

The specific meaning of some important characters is listed below for a quick reference. This list follows the similar fashion of characters usage in the "Computational methods for plasticity: theory and applications" (de Souza Neto, Perić, & Owen, 2008).

1.2.1 Important variables

$\mathbf{B}$	Generic finite element symmetric gradient matrix
$\mathbf{b}$	Generic body force vector
c	Cohesion
$\mathbf{D}$	Consistent tangent matrix
$\mathbf{D}^{e}$	Elasticity tangent matrix
$\mathbf{D}^{ep}$	Elastoplastic consistent tangent matrix
D	The unit tensor parallel to elastic trial deviatoric strain tensor
E	Young's modulus
$\mathbf{f}^{ext}$	Global (finite element) external force vector
$\mathbf{f}_{e}^{ext}$	External force vector of element e
$\mathbf{f}^{int}$	Global (finite element) internal force vector
$\mathbf{f}_{e}^{int}$	Internal force vector of element e
G	Shear modulus
H	Linear isotropic hardening modulus
I	Fourth-order identity tensor

I_T Fourth-order transposition tensor

I Second-order identity tensor

I_s Fourth-order symmetric identity tensor: $\mathrm{I}_s = \frac{1}{2}\left(\mathrm{I} + \mathrm{I}_T\right)$

I_d Fourth-order deviatoric projection tensor: $\mathrm{I}_d \equiv \mathrm{I}_s - \frac{1}{3} I \otimes I$

J_2 Second invariant of deviatoric stress

K Bulk modulus

$\mathbf{K}$ Global stiffness matrix

$\mathbf{K}^e$ Stiffness matrix of element e

$\mathbf{k}$ Vector of hardening parameters in yield function

$\mathbf{m}$ Vector of state parameters in plastic potential function

$\mathbf{N}$ Generic shape functions tensor

$\boldsymbol{N}$ Plastic flow vector

p Mean stress or hydrostatic stress

q An invariant of deviatoric stress tensor, $q = \sqrt{3J_2}$

p_{pi} Initial pore pressure

p_w Wellbore pressure

R_e Reservoir radius

R_w Wellbore radius

$\mathbf{s}$ Deviatoric stress tensor

$\mathbf{t}$ Generic surface traction vector

u Generic displacement vector

$\mathbf{u}$	Global finite element nodal displacement vector
α	Generic internal state variables
α^{trial}	Trial generic internal state variables at elastic trial step
Λ	Plastic multiplier
η, ξ	Material parameter for Drucker-Prager yield function
$\bar{\eta}$	Material parameter for non-associative Drucker-Prager flow rule
ε	Generic strain tensor
$\boldsymbol{\varepsilon}$	Strain tensor in array form
$\boldsymbol{\varepsilon}^{e\,trial}$	Trial elastic strain tensor at elastic trial step
ε^{e}	Generic elastic strain tensor
ε^{p}	Generic plastic strain tensor
$\bar{\varepsilon}^{p}$	Accumulated (or equivalent) plastic strain, scalar
λ	First lame constant
ν	Poisson ratio
Φ	Yield function
Ψ	Plastic potential function
σ	Generic stress tensor
σ'	Generic effective stress tensor
$\boldsymbol{\sigma}$	Stress tensor in array form
Ω	Domain of a body in the reference configuration

1.2.2 Some important operational symbols

$tr(\cdot)$	Trace of $(\cdot)$

$\mathrm{d}(\cdot)$ Differentiation of $(\cdot)$

$\Delta(\cdot)$ Generic change of $(\cdot)$

$\delta(\cdot)$ Iterative increment of $(\cdot)$

$\partial(\cdot)$ Boundary of the domain $(\cdot)$

$\partial_a(\cdot)$ Subdifferential of $(\cdot)$ with respect to a

$\frac{\partial}{\partial a}(\cdot)$ Derivative of $(\cdot)$ with respect to a

$\mathbf{S}:\mathbf{T}$ Inner product of second-order tensors

$\mathbf{S}\otimes\mathbf{T}$ Tensor product of tensors

$\|(\cdot)\|$ Euclidean norm

Chapter 2 Literature Review

Wellbore stability analysis started from purely a mechanical study of the stress distribution around a newly drilled vertical wellbore. The stress state of rock in the underground is in equilibrium before a well is drilled. However, the stress state in the region near the wellbore is disturbed, as the support originally offered by the drilled out rock is replaced by the wellbore pressure (McLean & Addis, 1990). And the rock region fails when the redistributed stress state reaches the failure surface. Given the cause of instability, the analysis of wellbore stability entails two aspects, modeling rock deformation behavior, and compatible failure criterion. Comprehensive reviews of these two elements are referred to the work in 1990 by McLean et al. and that in 2009 by Kang et al.

The first published results of the stress distribution were presented by Bradley using the linear elastic model under the plane strain assumption (W. B. Bradley, 1979; W. B Bradley, 1979). From then on, many published constitutive models have been used to solve the wellbore stability problem. The constitutive models can be generally categorized into two groups: single-physics and multi-physics. This study focuses on single-physics only, while fluid flow, clay swelling and thermal effects, etc. are beyond the scope of the work.

First, within the platform of the linear elasticity, researchers have developed a series of wellbore stability analysis with respect to wellbore inclination, azimuth, anisotropic rock properties, and in-situ stress regimes. The influence of inclination angle on the risks of both collapse failure and fracturing failure of inclined wells was studied by the linear elastic model for isotropic materials in combination with multiple failure criteria (B. S. Aadnoy & Chenevert, 1987). Aadnoy found that the wellbore becomes more sensitive to collapse with the increasing inclination angle. On the contrary, the fracture pressure gradient generally decreases with the increasing

inclination angle. In the same year, another study was conducted for inclined wells in anisotropic rocks (B.S. Aadnoy & hogskole, 1987). On the basis of above works, the impact of different stress regimes on the wellbore stability was investigated for both horizontal wells and deviated wells (Hsiao, 1988; Zhou, Hillis, & Sandiford, 1996). They derived similar conclusions that stress regimes have a significant influence on the wellbore stability analysis. For the extensional stress regime (the maximum principal stress is the vertical stress) the vertical well may not be the most stable wellbore profile compared to a deviated wellbore. In 2009, Al-Ajmi illustrated the same finding by studying the field experiences in the North Sea, Indonesia and Arabian Gulf (Al-Ajmi & Zimmerman, 2009).

However, rock properties are never nearly as simple as the linear elastic model predicts. Santarelli carried out a series of pseudo-triaxial tests on laboratory scale wellbores; however, the tested failure pressure is usually between 2 and 8 times larger than that predicted by the linear elastic model (Santarelli, 1987). It has been commonly accepted that the prediction obtained by the linear elastic model is very conservative and a plastic model is a technique to improve the accuracy of the prediction (McLean & Addis, 1990). In contrast to the linear elasticity, elastoplastic models have been rarely published due to the severe complexity of the algorithm and overwhelming cost of computation. Therefore, a more thorough review of the elastoplastic approach to the wellbore stability analysis is presented in this section. One of the earliest works pertaining plasticity is dated back to 1940 by a civil engineer (Westergaard & Malcolm, 1940). In his analysis, a section near the wellbore may enter the plasticity region and begin to flow. The post-failure behavior was not quantitatively studied because of the assumption of perfect plasticity. Before a more realistic elastoplastic study was published, Morita and Gray presented a nonlinear elastic constitutive model to study the stress state around the borehole up to failure (Morita & Gray,

1980). In their study, the stress-strain curve is divided into four stages: an initial non-linear portion, a linear portion, a final nonlinear portion, and the volume change of rock matrix by pore pressure. Their study concluded that the use of conventional linear stress-strain behavior renders significant error for well stability problems compared to the nonlinear model. Then Drucker-Prager yield criterion and Mohr-Coulomb yield criterion were adopted in the analysis under plane strain assumption (Veeken, Walters, Kenter, & Davies, 1989). A comparative study between the theoretical models and hollow cylinder tests was done, from which a good match in the failure pressure was found. Also, the calculated softening regions and hardening regions, which were depicted to show the wellbore failure, show good agreement with hollow cylinder test results. However, as inferred by Veeken et al., the match in collapse pressure is likely to be a coincidence rather than sound modelling.

Papanastasiou et al. went a step further by replacing the small strain assumption with large strain assumption in both Mohr-Coulomb yield criterion and inscribed Drucker-Prager yield criterion (Papanastasiou, Thiercelin, Cook, & Durban, 1994). In contrast to previous studies, the paper derived their analytical solution for a radially stressed hollow cylinder under axially symmetric plane strain assumption because they contended that analytical solution or semi-analytical solution is still valuable for quick solutions in real time. The analytical solutions have good accuracy compared with the thick cylinder tests results. Furthermore, they mentioned that hollow cylinder strength is scale-dependent and this effect should be studied further before a theoretical model can more accurately predict the stability of field-scale wellbore. Zervos et al. extended the study to 3D for the analysis in deviated wells (Zervos, Papanastasiou, & Cook, 1998). They utilized the inscribed Drucker-Prager yield criterion for an inclined well in combination with the numerical solution by finite element method. As a result, they found that the relative difference

in predicted mud weight varies from 45% to 80% between the elasticity model with a peak-strength failure criterion and Drucker-Prager yield criterion with a strain-based failure criterion. Fung et al. addressed more details in the algorithm of the finite element method for a nonlinear elastoplastic problem (Fung, Wan, Rodriguez, Silva Bellorin, & Zerpa, 1999).

Inspired by the finding of scale effect on the strength of thick-walled cylinders, Zervos et al. published another paper on the scale effect and localization with the help of gradient elastoplasticity (Zervos, Papanastasiou, & Vardoulakis, 2001). They found that the in the thick-walled cylinders tests, the load required to initiate failure seems to be larger for small holes than for large holes. They also studied the post-peak behavior, which is marked by the progressive localization of deformation, by including strain-softening effect. More studies on the micromechanisms of borehole instability have been published in the recent decade. Haimson experimentally studied the micromechanism of breakout failure in a variety of granites, limestones and sandstones under a wide range of pre-existing stress fields (Haimson, 2006). Besides what researcher used to know about the dog-eared breakouts along the minimum horizontal far-field stress springline in vertical wells through various rocks due to shear-dilation, he declared that a new type of failure was discovered in quartz-rich sandstones under the analysis of optical and scanning electron microscopes, where tabular slot-shaped breakouts developed. The breakouts maintain a constant very narrow width over an extensive length, resulting in a fracture-like appearance due to compaction. Spieza el al. recently adopted a numerical approach to study both shear-induced dilation and shear-enhanced compaction failure mechanism by means of a cap model (Spiezia, Salomoni, & Majorana, 2015). The cap model consists of two smoothly intersecting yield surfaces, which permits different failure modes. The results of the study show that a wellbore can experience both compactant and dilatant plasticity under certain conditions

mostly defined by the in-situ stress condition and the mud pressure. They concluded that the conventional model which only models the dilatant plasticity underestimates the extension of plastic zone around the wellbore.

Back to the second element in the analysis, failure criteria are reviewed briefly in this section. At early stage, rock failure is determined using a peak-strength failure criterion that is normally defined in terms of principal stresses (McLean & Addis, 1990). Failure occurs once the stress state reaches the critical peak-strength of the rock. On the platform of elasticity, yield criterion is the same as failure criterion (i.e., yield of rock marks the failure of rock). However, this is contradictory to what is observed in the field. Because in many cases the borehole remains stable even if the stress concentration around the wellbore has exceeded the elastic limit of the formation (Salehi, Hareland, & Nygaard, 2010). From this respect, the elastoplastic model offers the ability to evaluate the mechanical integrity of a borehole more realistically, since it can model the evolution of rock deformation after the initial yield point. The criterion to predict the failure during the plastic straining is still debatable. Some researchers used peak-strength criterion and some adopted plastic strain-based criterion. The peak-strength and the critical strain value is usually calibrated from laboratory tests like a triaxial test. Considering the reality in drilling operation, the critical plastic strain has been defined based on the requirement of specific service, like avoiding stuck pipe in drilling service as well (Fung et al., 1999; Zervos et al., 1998). As the material yields, the bounding force between the grains is weakened. In other words, the yielded zone becomes more susceptible to spalling due to the artificial effect, like pressure surges during trips and mechanical erosion by the drillstring (Hawkes & McLellan, 1996). Hawkes and Mclellan then proposed a criterion to assess the risk of wellbore instability based on the area of yielded zone.

There are a small number of papers on the elastoplastic approach for the wellbore stability analysis; most of them were focused on the theoretical model, while practical application to field cases are rarely seen as a result of both the high computation cost involved and difficulties in acquiring various material parameters for an elastoplastic model in real field cases. The computing efficiency has been boosted by several orders of magnitude in the past decades, which makes complex computations more feasible. It should be emphasized that the flexibility and clarity of the finite element analysis code has been largely improved by taking advantage of the object-oriented programming (Dubois-Pèlerin, Zimmermann, & Bomme, 1992; Mackie, 1992, 2001; Zimmermann, Dubois-Pèlerin, & Bomme, 1992). The advantage of taking object-oriented philosophy to program the finite element methods were well discussed. Mackie's paper is dedicated to explaining the benefits of object-oriented programming to the finite element method from the aspect of modularity of both the object-oriented programming philosophy and the finite element method. A prototype program was also provided by the paper of Dubois-Pèlerin et al. in Smalltalk. Later on the nonlinear finite element analysis using object-oriented philosophy was addressed with an application to beam elements and the cosserat continuum (Paulino, 1999).

This project is designed to provide a numerical technique to guide the wellbore stability analysis in the drilling industry with a more realistic strain hardening elastoplastic model. The study is aimed at investigating the failure mechanism by observing the extension of the plastic zone inside the wellbore boundary rather than focusing on the boundary only. Looking at the plastic yield zone inside the wellbore will offer the drilling engineer a new perspective to investigate the wellbore stability problem.

Chapter 3 Problem Definition and Assumptions

The problem is defined in this section followed by a generally explained methodology.

3.1 Problem definition

This section generalizes the wellbore drilling process to two stages, before drilling and after drilling. Initially, uniform stress filed is assumed for the formation at certain depth before drilling, as labeled in Figure 3-1. The direction of vertical stress σ_v and the direction of the maximum horizontal stress σ_H define a random plane at this depth. The direction of the minimum horizontal stress σ_h is normal to the plane. A Cartesian coordinate system is set up on the plane, where the x-axis is along the direction of σ_h and the y-axis is along the direction of σ_v.

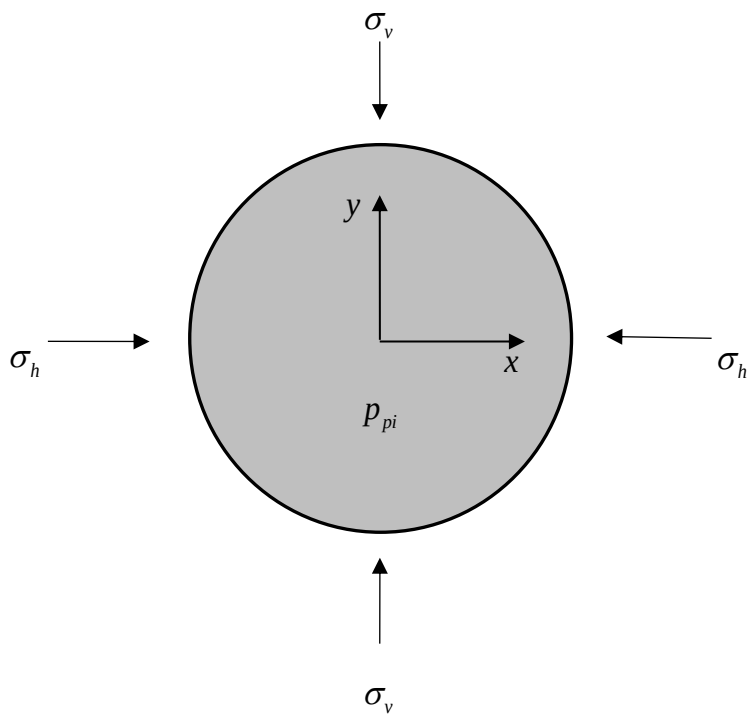

Figure 3-1. The cross section of the formation before drilling

Second, a long straight horizontal wellbore is drilled in the shown formation with wellbore pressure p_w in Figure 3-2. The near wellbore region deforms due to the imbalanced forces but the in-situ stress is not affected in far field. Because of the uncertainty of the direction of the in-situ stress, the well is assumed at the worst situation to maintain wellbore stability, i.e., along the direction of the maximum horizontal stress in that the wellbore suffers the most severe deviatoric stress. At the section of interest, the wellbore is open-hole and drained condition is assumed. So the pore pressure remains p_{pi} throughout the simulation.

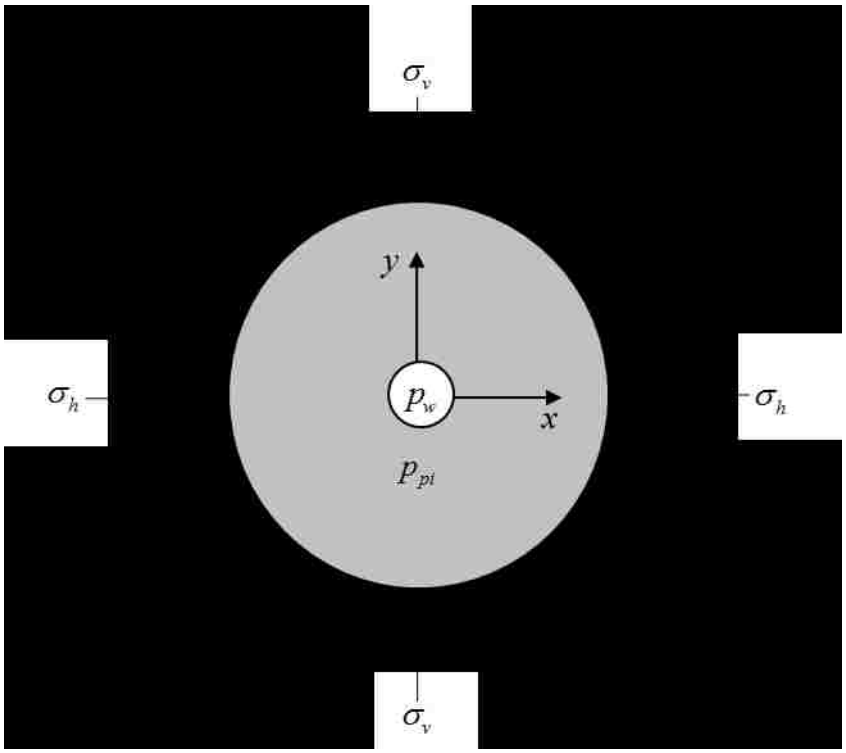

Figure 3-2. The cross section of the formation with a horizontal well

The deformation of rock in the near wellbore region is to be analyzed, based on which a prediction of wellbore stability is to be given.

3.2 List of assumptions

1. The loss of mechanical equilibrium causes the deformation and failure of wellbore. No fluid flow, thermal effects, chemical effects and man-made effects are considered during the drilling process. The only hydraulic effect of the drilling mud is to provide hydrostatic pressure support to the borehole surface.
2. The material properties are assumed homogeneous and isotropic.
3. Drained condition is assumed so that the pore pressure change is ignored. Effective stress is used to account for pore pressure.
4. A finite external boundary is large enough to maintain the original in-situ stress on the boundary.
5. Plane strain idealization is used to simplify the problem to 2D because the stress in the length direction is considered to be a constant value. The variation of overburden stress over the domain of interest is ignored.
6. The wellbore failure is resulted by dilatant shear failure only.
7. The likelihood of wellbore instability is dependent on the area of yielded zone. The larger the yielded zone, the more risk to have wellbore instability problems.
8. The non-shale formation is a strain hardening Drucker-Prager material. The linear hardening rule is further assumed for the simplicity in computation.

Chapter 4 Methodology

This chapter elaborates on the methods used for this wellbore stability problem. Essentially, the problem is modeled by non-associative Drucker-Prager model and then solved by nonlinear finite element method. Thus the chapter starts from the introduction on the theory of general elastoplastic model. This introduction covers the most fundamental ideas of the elastoplastic theory which can help differentiate it from the pure elastic theory. Then the non-associative Drucker-Prager model is introduced and the formulation is addressed. Next section explains the nonlinear finite element methods tailored for the problem. Following the general theory, the finite element formulation of non-associative Drucker-Prager model is derived in the next section. This section is the most important part in this chapter as the code is directly programmed on the basis of the formulations derived there. Finally, the structure of the program NSMOOM is briefly explained in the last section for readers who are interested in extending or changing the code. This fundamentals in chapter are mainly borrowed from the two classic books: "Finite element analysis in geotechnical engineering," by David, M. Potts, 1999; and "Theory and Applications," by de Souza Neto et al., 2008.

4.1 General elastoplasticity theory

This section begins with the uniaxial behavior of a linear elastic-plastic material. Then the basic ingredients of elastoplastic theory is introduced and the consistency between those ideas and real soil behavior is shown. The basic concepts for a general elasto-plastic model addressed here will be inherited by most elasto-plastic models, including Drucker-Prager model in the next section.

4.1.1 Real rock behavior

The real rock behavior under uniaxial compression is shown in Figure 4-1 by a stress-strain curve(David, 1999). One can easily notice that the strain increments are almost proportionally

increasing with the stress increment in the beginning state, which is well known as elastic stage. However, strain increments are no longer linearly related to stress after certain point which we call yield point. The stress value at this yield point is defined as yield stress. After yield point, rock enters the plastic stage.

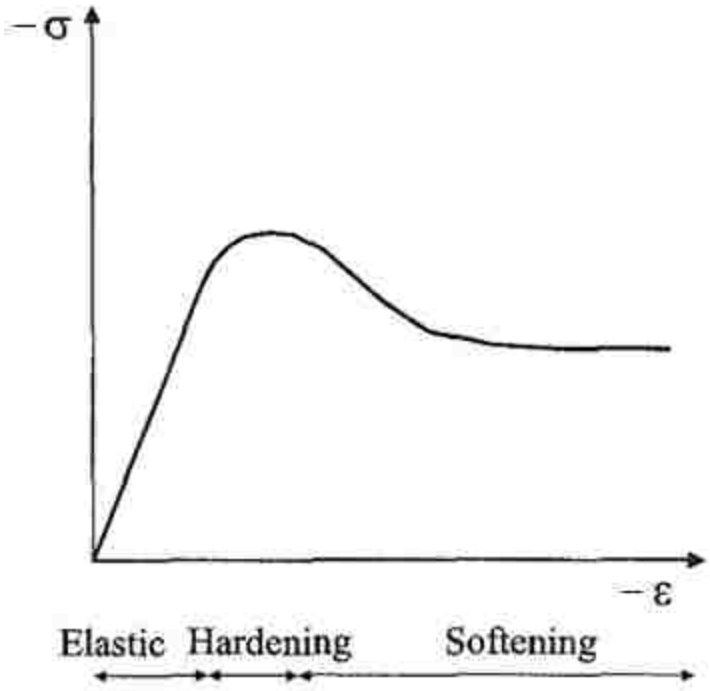

Figure 4-1 Stress-strain curve of real rock under uniaxial compression. Source: "Finite element analysis in geotechnical engineering," by David, M. Potts, 1999, Thomas Telford Publishing, p.142.

The slope of stress-strain curve first decreases which means strain continues increasing while stress doesn't increase as fast as it does in the elastic stage. In other words, rock is losing its modulus gradually due to the accumulated strain. This stage is called strain hardening. Keeping the load on the rock during hardening stage will eventually lead to a new stage when rock cannot take anymore load. The new stage is called strain softening. In the beginning zone of softening stage, the stress drastically decreases as the excessive strain weakens the rock dramatically. However, the stress will not decrease to zero but keep at a low value when the strain keeps

developing. The low value is called residual strength by some textbooks. While traditional constitutive models only model the first elastic stage, the elasto-plastic model can also capture the nonlinear rock behavior.

In the foregoing discussion, linear elasticity is assumed. In reality, elastic behavior is not necessarily linear while a nonlinear elastic session appears in the beginning. However, the non-linear section disappears when the confining stress is of a high value, which is usually the case in drilling. Though this thesis doesn't account for the nonlinear elastic behavior, it is possible to incorporate the nonlinear section into the elasto-plastic framework.

4.1.2 Basic ingredients of general elastoplastic model (David, 1999)

Elastoplastic models were derived on the basis of several assumptions. The following four assumptions are usually indispensable to formulate an elastoplastic model.

1. Coincidence of axes

The principal directions of incremental plastic strain are assumed to be parallel to those of total stress. This assumption is different in the elastic theory, where the principal directions of incremental strain and incremental stress coincide.

2. Yield functions

In the uniaxial situation discussed in the above section, yield point indicates the onset of plastic straining. Yield point is also a function of hardening parameter. In the multi-axial case, a yield surface instead of a yield point defines the boundary of elastic domain. In Figure 4-2, within the surface, the stress state is within the elastic domain. Once the stress state reaches the surface, plastic straining begins and stress state will stay on the yield surface, which is known as the consistency condition.

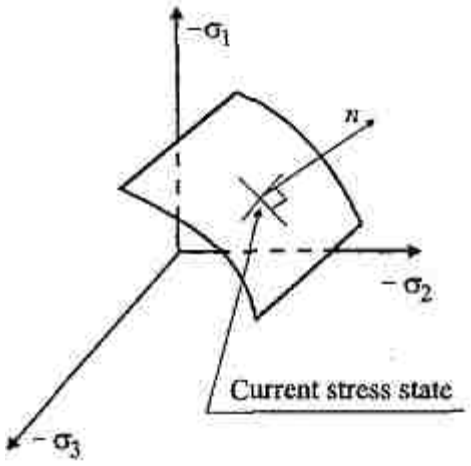

Figure 4-2 Yield surface in principal stress space. Adapted from: "Finite element analysis in geotechnical engineering," by David, M. Potts, 1999, Thomas Telford Publishing, p.138.

The yield surface is mathematically represented by a scalar function of stress state σ and hardening parameters $\mathbf{k}$. This function is called the yield function which takes the form as follows.

$$\Phi(\sigma, \mathbf{k}) = 0 \tag{4.1}$$

Stress state σ can be expressed in terms of stress components or stress invariants. Hardening parameters $\mathbf{k}$ control the size of the yield surface. Hardening parameters $\mathbf{k}$ are related to hardening parameters or softening parameters which are usually plastic strains.

Then one can tell the type of material behavior by checking the value of the yield function. Purely elastic behavior occurs if $\Phi(\sigma, \mathbf{k}) < 0$, and plastic behavior occurs when $\Phi(\sigma, \mathbf{k}) = 0$. The space enclosed by the yield surface is defined as the elastic domain. Note that $\Phi(\sigma, \mathbf{k}) > 0$ indicates an impossible situation, i.e., the stress state can never be located above the yield surface which is denoted by the outward normal vector n in Figure 4-2. And the consistency condition can be mathematically expressed as

$$\mathrm{d}\Phi(\sigma, \mathbf{k}) = 0 \tag{4.2}$$

There is not necessarily only one yield surface to determine the material behavior. Actually multi-surface elasto-plastic models are very common. The most well-known elasto-plastic model to petroleum engineers, the yield surface of Mohr-Coulomb model contains six planes in the principal stress space and Drucker-Prager cap model is a multi-surface model as well. Therefore, multiple yield functions are formulated to represent the multi-surface model.

3. Plastic potential functions and flow rule

Yield function provides a way to check the type of material behavior. It is straightforward to use elastic constitutive equation to calculate the stress and strain in the elastic domain, however, both the direction and the magnitude of plastic strain cannot be solved by the knowledge discussed above once the stress state reaches yield surface. In the uniaxial example, it is self-explanatory that the plastic strains take place in the same direction as the exerted stress. Whereas, it is more complex in the multi-axial situation since there are actually six components of both stress and strain tensor. Therefore some means of specifying the direction and magnitude of plastic straining should be introduced for every stress state on the yield surface. This is done by means of a flow rule where the plastic potential functions are introduced. The flow rule can be expressed as follows:

$$\Delta\varepsilon_i^p = \Lambda \frac{\partial \Psi\left(\sigma, \mathbf{m}\right)}{\partial \sigma_i} \tag{4.3}$$

where, $\Delta\varepsilon_i^p$ means the components of the incremental plastic strain (in terms of either strain tensor or strain invariants), $\Psi\left(\sigma, \mathbf{m}\right)$ is the so called plastic potential function or flow potential function and Λ is a positive scalar multiplier which controls the magnitude of plastic strain. The plastic potential function takes the similar form of the yield function:

$$\Psi(\sigma, \mathbf{m}) = 0 \tag{4.4}$$

where, $\mathbf{m}$ is a vector of state parameters which are not material properties. The plastic potential function defines a plastic potential surface in the stress space.

The differential of $\Psi(\sigma, \mathbf{m})$ with respect to stress components defines the relative magnitude of plastic strain components, which is essentially the direction of plastic strain increment. The plastic strain multiplier Λ which controls the absolute magnitude is the key to solve the elastoplastic models. However, its value is not definite with the knowledge mentioned above. Whereas, it is solvable either explicitly or implicitly with the assistance of the hardening rule or softening rule which will be discussed later.

Note that the plastic potential function is postulated to predict the plastic straining once the stress state reaches the yield surface. Therefore it is sometimes assumed that the plastic potential function takes the same form of the yield function, i.e., the yield surface and plastic potential coincide. In this case, we call the flow rule associative (or associated). It is called non-associative (or non-associated) flow rule when the plastic potential function is different from the yield function. The non-associative flow rule is more general according to laboratory observations while associative flow rule is a simplification case which is usually more acceptable for ductile materials like ductile metals than others(de Souza Neto et al., 2008; Ledgerwood, 1988; Sandler, 2005). However, this simplification is very commonly used due to two drawbacks of the non-associative flow rule: the difficulty in obtaining parameters and the significant computation cost in finite element analysis.

4. The hardending /softening rule

From the above discussion, the yield surface is a function of both stress state σ and hardening parameters $\mathbf{k}$. The hardening parameter controls the size of yield surface and change in

the value of hardening parameters signifies the evolution of yield surfaces. When hardening occurs, the hardening parameters increase so that the yield surface expands. Whereas the hardening parameters decrease and yield surface shrinks when softening takes place.

The hardening/ softening rules quantitatively prescribe how the hardening parameters vary with the plastic straining so that the plastic multiplier Λ can be solved. Hardening rules most commonly relate the hardening parameter to an internal state variable. This type hardening/softening rule is called a strain hardening/softening. The evolution for the internal state variable α is obtained by

$$\Delta\alpha = -\Lambda \frac{\partial \Phi}{\partial \mathbf{k}} \tag{4.5}$$

Sometimes the hardening parameters $\mathbf{k}$ is postulated as a function of plastic work. Such hardening/ softening rules are called work hardening/ softening.

If the material is perfectly plastic, no hardening or softening takes place and hardening parameters $\mathbf{k}$ are constant. In this case, hardening/ softening rules are not required and the value of the multiplier Λ is not definite. The perfect plastic model can still be solved for a boundary value problem where all point are constrained by certain condition. However, the model cannot be solved for one isolated point which is not constrained.

4.2 Strain hardening Drucker-Prager model

Among the commonly used classic elastoplastic yield criteria, Mohr-Coulomb and Drucker-Prager models are most widely used in petroleum engineering and geotechnical engineering when dealing with rock deformation. The well-known Drucker-Prager yield criterion was originally proposed by Drucker and Prager to approximate Mohr-Coulomb criterion in 1952. Mohr-Coulomb is not dependent on the intermediate principal stress and is usually expressed in terms of two principal stresses. Sometimes the yield criterion is also formulated in terms of three stress

invariants. However, Drucker Prager model does account for three principal stresses but the third stress invariant, lode angle, disappears in the yield function when it is expressed in terms of stress invariants. Thus the yield locus of Drucker-Prager model in the deviatoric plane (the plane normal to the hydrostatic axis in the principal stress space) is a circle.

4.2.1 Yield function

Drucker-Prager model states that plastic yielding begins when J_2 invariant of the deviatoric stress $\mathbf{s}$ and the mean stress p reach a critical combination (de Souza Neto et al., 2008). In the $\sqrt{J_2} - p$ plane, the yield surface is a straight line for the classic Drucker-Prager model, which is formulated as follows:

$$\Phi(\sigma, c) = \sqrt{J_2(\mathbf{s})} + \eta p(\sigma) - \xi c = 0 \tag{4.6}$$

where, η and ξ are material parameters used to approximate Mohr-Coulomb model; c is cohesion inherited from Mohr-Coulomb model; and $\sqrt{J_2(\mathbf{s})}$ is the invariant of deviatoric stress which can be expressed as

$$\sqrt{J_2(\mathbf{s})} = \sqrt{\frac{1}{2} tr(\mathbf{s}^2)} = \sqrt{\frac{1}{2}\mathbf{s}:\mathbf{s}} = \sqrt{\frac{1}{2}}\|\mathbf{s}\| \tag{4.7}$$

and the deviatoric stress $\mathbf{s}$ is defined by

$$\mathbf{s} = \sigma - pI \tag{4.8}$$

where, I is the identity tensor is the p as the mean stress or hydrostatic stress is defined as

$$p = \frac{1}{3}(\sigma_1 + \sigma_2 + \sigma_3) \tag{4.9}$$

Represented in the principal stress space, the yield locus of this yield criterion is a circular cone whose axis is the hydrostatic line, as illustrated in Figure 4-3. $\sqrt{3}p$ near the hydrostatic line denotes that the distance from the center of the circle to the origin of the coordinate system.

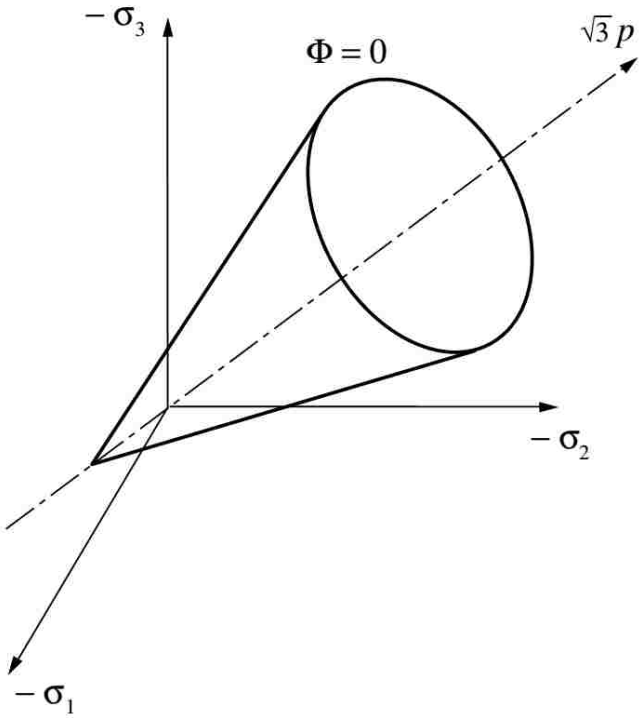

Figure 4-3 Drucker-Prager yield surface in principal stress space. Adapted from "Computational Methods for Plasticity: Theory and Applications," by de Souza Neto et al., 2008, John Wiley & Sons, Ltd, p.167.

Given that the yield surface of Mohr-Coulomb model is an irregular hexagonal pyramid, two of the most common approximations used are obtained by selecting a set of η and ξ to make the yield surfaces of Drucker-Prager and Mohr-Coulomb criteria coincident either at the outer or inner edges of Mohr-coulomb surface. The approximation is clearly illustrated on the π plane (or the deviatoric plane) in Figure 4-4.

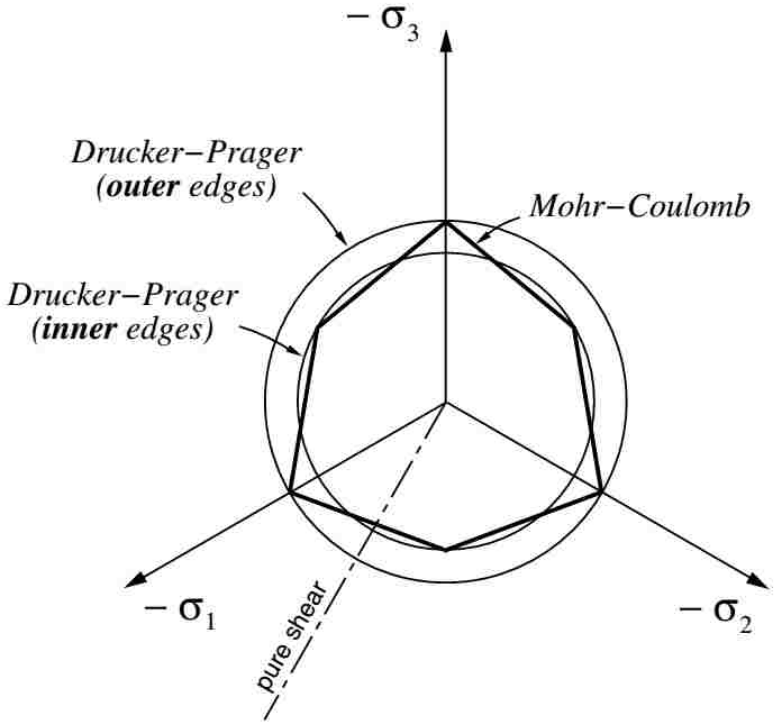

Figure 4-4 Yield surfaces of Drucker-Prager and Mohr-Coulomb model on the π plane. Adapted from: "Computational Methods for Plasticity: Theory and Applications," by de Souza Neto et al., 2008, John Wiley & Sons, Ltd, p.169.

The outer edge approximation matches Mohr-Coulomb criterion in uniaxial compression and biaxial tension cases. So the outer cone is known as the compression cone. Coincidence at the outer edges is obtained when

$$\eta = \frac{6\sin\phi}{\sqrt{3}(3-\sin\phi)}, \quad \xi = \frac{6\cos\phi}{\sqrt{3}(3-\sin\phi)} \tag{4.10}$$

where ϕ is the internal friction angle inherited from Mohr-Coulomb model.

Whereas, the inner cone is called the extension cone because it matches Mohr-Coulomb model in uniaxial tension and biaxial compression experiments. The coincidence at the inner edges is given by the choice

$$\eta = \frac{6\sin\phi}{\sqrt{3}(3+\sin\phi)}, \quad \xi = \frac{6\cos\phi}{\sqrt{3}(3+\sin\phi)} \tag{4.11}$$

The thesis select another well-known approximation because the objective of the thesis is to study the wellbore stability. The type of approximation is to have both criteria predict the same collapse loads under plane strain condition (Chen & Mizuno, 1990), which is very appropriate for the wellbore problem. The set of η and ξ are expressed as

$$\eta = \frac{3\tan\phi}{\sqrt{9+12\tan^2\phi}}, \quad \xi = \frac{3}{\sqrt{9+12\tan^2\phi}} \tag{4.12}$$

Note the apex of the three approximating Drucker-Prager yield cone coincides with the apex of the corresponding Mohr-Coulomb yield surface. Also one should be reminded that any of the above three approximations is not universally applicable to arbitrary loading conditions. They may produce poor predictions at certain stress states. The discussion on the performance of the approximations of Drucker-Prager model to Mohr-Coulomb model can be found in works by Chen and Mizuno and Zienkiewicz et al. (Chen & Mizuno, 1990; Zienkiewicz, Norris, Winnicki, Naylor, & Lewis, 1978).

4.2.2 Plastic potential functions and flow rule

From section 4.1.2 , one already knows that flow rule is associative if the plastic flow function is identical to the yield function. Associative flow rule is simple to define and less computation intensive. However, its performance for Drucker-Prager model has been criticized by many researchers complaining that it predicts the irrational dilatant plastic strain (Sandler, 2005). Therefore this thesis will assume non-associative flow rule from the beginning. The importance of doing so is one easily adapt the formulation or numerical code to associative flow rule by setting the flow function and the yield function the same.

1. Associative flow rule

The plastic potential function is the same as the yield function, therefore

$$\Psi(\sigma, c) = \sqrt{J_2(\mathbf{s})} + \eta p(\sigma) - \xi c = 0 \tag{4.13}$$

The evolution of plastic straining is formulated by the flow rule:

$$\Delta\varepsilon^p = \Lambda \boldsymbol{N} \tag{4.14}$$

where Λ is the plastic multiplier and $\boldsymbol{N}$ is the flow vector. On the smooth cone, it is defined by

$$\boldsymbol{N} = \frac{\partial \Psi}{\partial \sigma} = \frac{1}{2\sqrt{J_2(\mathbf{s})}}\mathbf{s} + \frac{\eta}{3} I \tag{4.15}$$

The flow vector $\boldsymbol{N}$ is split into deviatoric and volumetric parts by

$$\boldsymbol{N}_d = \frac{1}{2\sqrt{J_2(\mathbf{s})}}\mathbf{s}, \quad \boldsymbol{N}_v = \frac{\eta}{3} I \tag{4.16}$$

where $\boldsymbol{N}_d$ is the flow vector for the deviatoric strain, $\boldsymbol{N}_v$ denotes the volumetric strain.

At the apex, the flow vector is not definite due to singularity. The subdifferential of a function is introduced to generalize the derivative to functions which are not differentiable. According to section 6.5.3 of "Computational Methods for Plasticity: Theory and Applications", the flow vector is derived from the standard properties of subdifferential (Ralph Tyrell Rockafellar, 1970; R Tyrrell Rockafellar & Wets, 2009). The flow vector $\boldsymbol{N}$ is split into deviatoric and volumetric parts by

$$\boldsymbol{N}_d \in \partial_\sigma \sqrt{J_2(\mathbf{s})}, \quad \mathbf{N}_v = \frac{\eta}{3} I \tag{4.17}$$

where ∂_σ means the subdifferential with respect to σ.

2. Non-associative flow rule

The non-associative flow rule is a variant of associative rule where the friction angle ϕ is replaced by the dilatant angle ψ which is usually smaller. Thus the plastic potential function is

$$\Psi(\sigma, c) = \sqrt{J_2(\mathbf{s})} + \bar{\eta}\, p(\sigma) + d = 0 \tag{4.18}$$

where d is simply the intersection of the current potential locus and the deviatoric axis and $\bar{\eta}$ is calculated by replacing ϕ with ψ in the definition of η. For plane strain approximation,

$$\bar{\eta} = \frac{3\tan\psi}{\sqrt{9 + 12\tan^2\psi}}, \tag{4.19}$$

One can observe that the flow vector given by the non-associative flow rule differs from its counterpart only in the volumetric component, that is,

$$\boldsymbol{N} = \frac{\partial \Psi}{\partial \sigma} = \frac{1}{2\sqrt{J_2(\mathbf{s})}}\mathbf{s} + \frac{\bar{\eta}}{3} I \tag{4.20}$$

4.2.3 Hardening rule

In this thesis, strain hardening is adopted. The hardening parameter **k** is chosen as the cohesion c and the internal state variable α is chosen as the von Mises effective plastic strain $\bar{\varepsilon}^p$, which is also known by von Mises equivalent or accumulated plastic strain. The effective plastic strain is obtained by integration of the incremental effective plastic strain which is defined as

$$\Delta\bar{\varepsilon}^p = \sqrt{\frac{2}{3}\Delta\varepsilon^p : \Delta\varepsilon^p} \tag{4.21}$$

where $\Delta\varepsilon^p$ is the incremental plastic strain tensor.The strain-hardening model is formulated as

$$c = c\left(\bar{\varepsilon}^p\right) \tag{4.22}$$

For Drucker Prager model, the evolution of $\bar{\varepsilon}^p$ is then obtained by(4.5):

$$\Delta\bar{\varepsilon}^p = -\Lambda\frac{\partial \Phi}{\partial \mathbf{k}} = -\Lambda\frac{\partial \Phi}{\partial c} = \Lambda\xi \tag{4.23}$$

Normally, the hardening model is assumed linear, which means,

$$c\left(\bar{\varepsilon}^{p}\right) = c_0 + H\bar{\varepsilon}^{p} \tag{4.24}$$

where constant c_0 is the initial cohesion before any yielding and H is defined as the isotropic hardening modulus. Note that H varies for nonlinear hardening model. Also we can find that the perfect plasticity model can be recovered when H is set to 0.

4.3 Non-linear Finite element method—Newton-Raphson Method

Finite element method is the most powerful and popular numerical tool to solve complex partial differential equation system over complicated geometry in engineering. The basic idea behind the finite element method is the discretization of the continuous domain and the interpolation technique to approximate the whole domain by means of discrete nodes. The theory of finite element method cannot be elaborated within one single book. This thesis will just borrow a piece from it to solve the specific pseudo-static nonlinear rock deformation problem.

4.3.1 Quick review of finite element methods for linear constitutive models

The classic linear finite element method is briefly reviewed here. The detailed explanation of the finite element theory and explicit form of most matrices and vectors mentioned here are referred to the chapter 4 in the book by de Souza Neto et al.

In petroleum engineering and geotechnical engineering, the pseudo-static problem conventionally takes the nodal displacements as the primary unknowns in that stress and strain can be easily recovered from the nodal displacements. Then problem is essentially an equilibrium equation expressed by

$$\mathbf{f}^{\text{int}}(\mathbf{u}) - \mathbf{f}^{\text{ext}} = \mathbf{0} \tag{4.25}$$

where, $\mathbf{f}^{\text{int}}$ is global internal force vector, $\mathbf{f}^{\text{ext}}$ is the global external force vector and $\mathbf{u}$ is the global nodal displacement vector. They are defined as follows

$$\mathbf{f}^{\text{int}} = \int_{\Omega} (\mathbf{B}^{g})^{T} \boldsymbol{\sigma} \mathrm{d}v$$
$$\mathbf{f}^{\text{ext}} = \int_{\Omega} (\mathbf{N}^{g})^{T} \mathbf{b} \mathrm{d}v + \int_{\partial\Omega} (\mathbf{N}^{g})^{T} \mathbf{t} \mathrm{da} \tag{4.26}$$

where $\mathbf{B}^{g}$ is the global finite element symmetric gradient matrix also known as the strain-displacement tensor and $\boldsymbol{\sigma}$ is the stress tensor in the array form. In the second equation, $\mathbf{N}^{g}$ is the global shape function tensor; $\mathbf{b}$ and $\mathbf{t}$ are respectively the body force and traction force vector.

Stress in the finite element method scheme is formulated by

$$\boldsymbol{\sigma} = \mathbf{D}\boldsymbol{\varepsilon} \tag{4.27}$$

where $\mathbf{D}$ is the consistent tangent matrix, which is the matrix form of the fourth-order consistent tangent operator

$$\mathbf{D} \equiv \frac{\partial \boldsymbol{\sigma}}{\partial \boldsymbol{\varepsilon}} \tag{4.28}$$

and $\boldsymbol{\varepsilon}$ is the strain tensor represented in array form. The strain as a function of displacements is expressed by

$$\boldsymbol{\varepsilon} = \mathbf{B}\mathbf{u} \tag{4.29}$$

Thus equation (4.26)[1] can be expanded as

$$\mathbf{f}^{\text{int}} = \int_{\Omega} (\mathbf{B}^{g})^{T} \boldsymbol{\sigma} \mathrm{d}v = \int_{\Omega} (\mathbf{B}^{g})^{T} \mathbf{D}^{g} \mathbf{B}^{g} \mathbf{u} \mathrm{d}v \tag{4.30}$$

As the nodal displacement vector $\mathbf{u}$ is not to be integrated, the equation can be expressed in terms of the global stiffness matrix $\mathbf{K}$ by

$$\mathbf{f}^{\text{int}} = \mathbf{K}\mathbf{u} \tag{4.31}$$

The global stiffness matrix $\mathbf{K}$ is assembled from the element stiffness matrix $\mathbf{K}^{e}$, which is

$$\mathbf{K}^{e} = \int_{\Omega^{e}} \left(\mathbf{B}^{e}\right)^{T} \mathbf{D}^{e} \mathbf{B}^{e} \mathrm{d}v \tag{4.32}$$

Finally, the equilibrium equation (4.25) becomes the following linear system of algebraic equations for the global nodal displacement vector $\mathbf{u}$:

$$\mathbf{Ku} = \mathbf{f}^{\text{ext}} \tag{4.33}$$

4.3.2 Finite element method for nonlinear constitutive models

The above discussion about the stress-strain relationship is for linear constitutive equations, like the linear elastic constitutive model. According to the constitutive equation, the stress tensor is a function of the instantaneous value of the infinitesimal strain tensor but not the history of the strain to which the material has been subjected. This kind of constitutive model is called path-independent. However, for the stress-strain relationship for elastoplastic models, the stress is dependent on the history of strain as well, thus the tangent matrix is not constant any more. This kind of constitutive model is called path dependent. The history of the strain is usually recorded by a set of internal state variables α, which is some kind of accumulation of strain increments.

For such path-dependent material, due to the nonlinearity, one can no longer establish the equilibrium equation in terms of total displacement and total force vector. The total load is now divided into several small load increments. For the $(n+1)^{th}$ load increment, the internal state variables α_n at the beginning of the increment and the strain tensor $\boldsymbol{\varepsilon}_{n+1}$ at the end of the increment are given. The stress $\boldsymbol{\sigma}_{n+1}$ at the end should be determined through an integration algorithm. Such an algorithm should give an approximation for $\boldsymbol{\sigma}_{n+1}$

$$\boldsymbol{\sigma}_{n+1} = \hat{\boldsymbol{\sigma}}\left(\alpha_n, \boldsymbol{\varepsilon}_{n+1}\right) \tag{4.34}$$

where $\hat{\boldsymbol{\sigma}}$ is the approximation for $\boldsymbol{\sigma}_{n+1}$. The approximation is expected to converge to the true solution when the size of the increment is small enough. Also note that α_n keeps being constant within one increment, i.e., the non-linear finite element method sets the constitutive law as path-

independent within one increment. The internal state variable get updated at the end of the increment through a similar integration algorithm

$$\alpha_{n+1} = \hat{\alpha}\left(\alpha_n, \boldsymbol{\varepsilon}_{n+1}\right) \tag{4.35}$$

Now, the incremental equilibrium equation for the $\left(n+1\right)^{th}$ increment can be expressed as

$$\mathbf{r}\left(\mathbf{u}_{n+1}\right) \equiv \mathbf{f}^{\text{int}}(\mathbf{u}_{n+1}) - \mathbf{f}_{n+1}^{\text{ext}} = 0 \tag{4.36}$$

where $\mathbf{r}\left(\mathbf{u}_{n+1}\right)$ is the global vector of residual nodal forces, $\mathbf{u}_{n+1}$ is the global nodal displacement vector at $\left(n+1\right)^{th}$ increment, $\mathbf{f}^{\text{int}}(\mathbf{u}_{n+1})$ and $\mathbf{f}_{n+1}^{\text{ext}}$ assembled from the element vectors

$$\mathbf{f}_{n+1}^{(\text{e})\text{int}} = \int_{\Omega^e} (\mathbf{B}^e)^T \hat{\boldsymbol{\sigma}}\left(\alpha_n, \boldsymbol{\varepsilon}_{n+1}\right) \mathrm{d}v \tag{4.37}$$

$$\mathbf{f}_{n+1}^{(\text{e})\text{ext}} = \int_{\Omega^e} (\mathbf{N}^e)^T \mathbf{b}_{n+1} \mathrm{d}v + \int_{\partial\Omega^e} (\mathbf{N}^e)^T \mathbf{t}_{n+1} \mathrm{da} \tag{4.38}$$

where $\mathbf{b}_{n+1}$ and $\mathbf{t}_{n+1}$ are the accumulated body force vector and traction force by the $\left(n+1\right)^{th}$ increment. The incremental equilibrium equation can also be expressed in a similar form of equation (4.33) by

$$\mathbf{K}\delta\mathbf{u}^{(k)} = -\mathbf{r}\left(\mathbf{u}_{n+1}^{(k-1)}\right) \tag{4.39}$$

where $\delta\mathbf{u}^{(k)}$ is the change of displacement after the k^{th} iteration. The specific technique to iteratively solve the incremental equilibrium equation is explained below.

4.3.3 Nonlinear solution--The Newton-Raphson algorithm

Last subsection infers that the solution for nonlinear constitutive models should come from cutting the total loads into several sufficiently small increments. There are many strategies to solve the incremental equilibrium equations. Top three popular solution algorithms are the tangent stiffness, the visco-plastic and Newton-Raphson schemes (David, 1999). The comparison done by David shows that the former two schemes are sensitive to the increment size and very inaccurate

predictions can be made when the increment size is large while the Newton-Raphson is consistently shown as the most robust. So the thesis takes advantage of the Newton-Raphson algorithm to solve nonlinear elastoplastic models.

"Substepping" and "return-mapping" methods are widely adopted and tested Newton-Raphson schemes which can be seen in various works (Borja, Sama, & Sanz, 2003; David, 1999; de Souza Neto et al., 2008; Simo & Hughes, 1998; Zhang, Hopperstad, Holmedal, & Dumoulin, 2014). While both algorithms can give relatively accurate results, the relative efficiency of these two methods haven't been quantitatively evaluated to the author's knowledge. For this project, the selection is mainly dependent on the simplicity of programing. Substepping method is an explicit algorithm and thus easy to develop the formulation for various constitutive models. While substepping method also gives relatively accurate results, the algorithm is usually lengthy and less commonly used. On the other hand, return-mapping method has been mostly adopted in textbooks and papers even though it takes effort to develop the formula for every kind of constitutive model. Fortunately, such formulations for classical elastoplastic models have been addressed in details in the book by de Souza Neto et al. and the book by Simo and Hughes.

The general Newton-Raphson algorithm is explained here and the formulations for the non-associative Drucker-Prager model will be addressed in the next section.

The Newton-Raphson algorithm is an iterative algorithm which entails iterations over one increment until the convergence. As shown in Figure 4-5, the internal nodal force vector $\mathbf{f}^{\text{int}}$ is approaching the external nodal force vector $\mathbf{f}_{n+1}^{\text{ext}}$ as the iteration goes on. This informative figure depicts how the scheme works for one increment by taking the $(n+1)^{th}$ increment as an example.

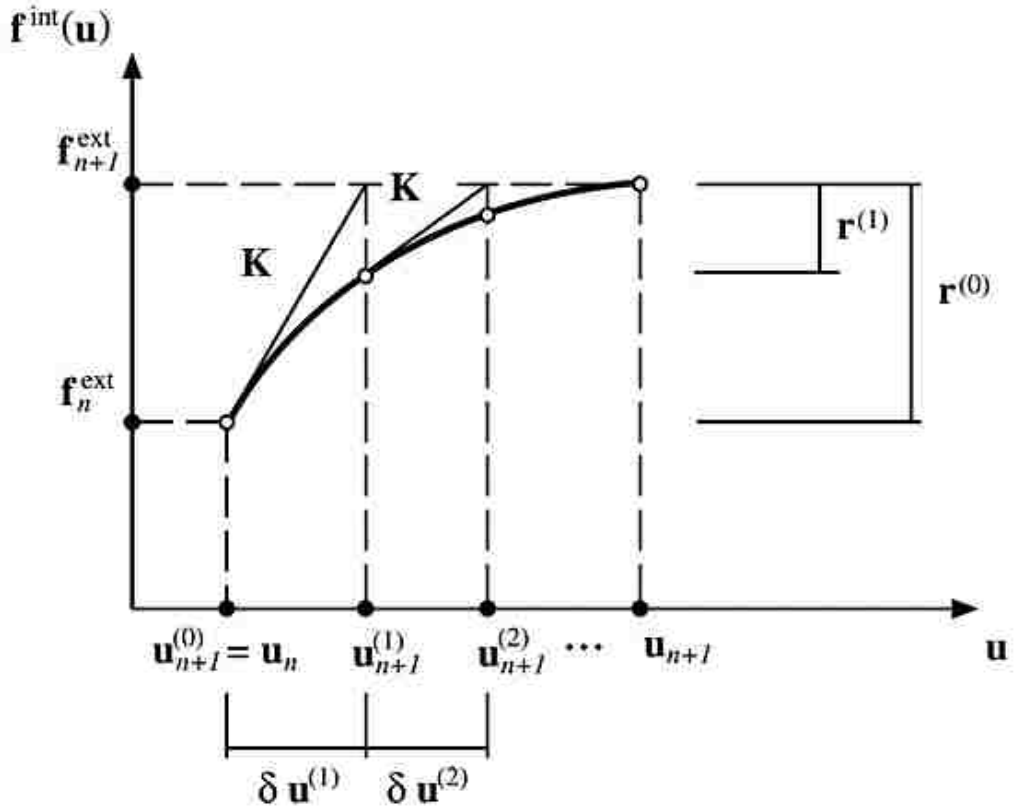

Figure 4-5 The Newton-Raphson algorithm for the incremental finite element equilibrium equations. Source: "Computational Methods for Plasticity: Theory and Applications," by de Souza Neto et al., 2008, John Wiley & Sons, Ltd, p.99.

At the end of n^{th} increment, the internal nodal force vector converges to the external nodal force vector $\mathbf{f}_n^{\text{ext}}$ so a new segment of external load is applied and the external force vector becomes $\mathbf{f}_{n+1}^{\text{ext}}$ and keeps constant during the $(n+1)^{th}$ increment. At the beginning of the first iteration, the internal nodal force vector $\mathbf{f}_{n+1}^{\text{int}(0)}$ is equal to $\mathbf{f}_n^{\text{ext}}$, then the residual nodal force vector is $\mathbf{f}_{n+1}^{\text{ext}} - \mathbf{f}_n^{\text{ext}}$. The total displacement $\mathbf{u}_{n+1}^{(0)}$ is the converged displacement vector $\mathbf{u}_n$ at the end of the n^{th} increment. The stiffness matrix was also calculated based on the stress state and internal state variable at the end of the n^{th} increment. Therefore, the incremental equilibrium equation (4.39) can be solved for the change of displacement $\delta\mathbf{u}^{(1)}$. Thus the total displacement $\mathbf{u}_{n+1}$ becomes $\mathbf{u}_{n+1}^{(1)}$ by

adding $\delta\mathbf{u}^{(1)}$ to $\mathbf{u}_{n+1}^{(0)}$. Then the strain is easily updated by taking advantage of the strain-displacement matrix $\mathbf{B}$. The key step is to update the stress state through integration over the strain path. From what we already know, this integration is numerically done by either the return-mapping or the substepping method. After the stress state is updated, the new internal nodal force vector $\mathbf{f}_{n+1}^{\text{int}(1)}$ is computed. So the residual nodal force vector is refreshed by equation (4.36) which is denoted by $\mathbf{r}^{(1)}$ in the figure. And after updating the stiffness matrix, the second iteration will follow the exact the same procedure as described for the first one. The iteration will continue until the convergence criterion is met.

The above explanation may work better in terms of equations for those familiar with the basis of the Newton-Raphson scheme. At a moment defined by the global displacement vector $\mathbf{u}_{n+1}^{(k-1)}$ after $(k-1)^{th}$ iteration, the k^{th} iteration of the scheme consists of the following procedures:

1. Update stress state and the residual nodal force vector

$$\mathbf{r}^{(k-1)} \equiv \mathbf{f}^{\text{int}}(\mathbf{u}_{n+1}^{(k-1)}) - \mathbf{f}_{n+1}^{\text{ext}} \tag{4.40}$$

2. Update the consistent tangent matrix and the stiffness matrix

$$\mathbf{K} = \int_{\Omega} \left(\mathbf{B}^{g}\right)^{T} \mathbf{D}\mathbf{B}^{g} \text{dv} = \left.\frac{\partial \mathbf{r}^{(k-1)}}{\partial \mathbf{u}_{n+1}}\right|_{\mathbf{u}_{n+1}^{(k-1)}} \tag{4.41}$$

3. Solve the linearized equation system (4.39) and get $\delta\mathbf{u}^{(k)}$, the change of displacement after the k^{th} iteration

4. Apply Newton correction to the global displacement

$$\mathbf{u}_{n+1}^{(k)} = \mathbf{u}_{n+1}^{(k-1)} + \delta\mathbf{u}^{(k)} \tag{4.42}.$$

5. Go back to the first step and perform another iteration until convergence criterion is satisfied.

It is important to emphasize that the described algorithm is here expressed in terms of whole domain, i.e., the global system. However, the actual programmed code starts the calculation from the Gaussian integration points. The stress, strain and the consistent tangent matrix are all on the Gaussian integration points for ease and accuracy of numerical simulation. The results on integration points are assembled to each finite element and the global system sequentially.

In addition to the first step of state updating, the second step is another key step in the Newton-Raphson scheme. The main idea is to update the consistent tangent matrix $\mathbf{D}$. In the scheme of return-mapping, it is defined as the derivative of the incremental constitutive function at the end of increment defined by the approximated stress state $\hat{\boldsymbol{\sigma}}$. That is why the return-mapping method is essentially an implicit algorithm. This implicit function has been solved by several numerical algorithm through linearization of the finite element equations for the path-dependent materials. Such algorithm should give the consistent tangent matrix $\mathbf{D}$ which is consistent to the stress update algorithm.

Note that in the standard Newton-Raphson scheme, the stiffness matrix is updated after each iteration. This standard Newton-Raphson has a quadratic rate of convergence. However, people want to reduce the time cost for updating the stiffness matrix. Traditionally, some set a constant stiffness matrix within each increment, i.e., the stiffness matrix is only updated at the beginning of the every increment (David, 1999). But the convergence rate and the overall solving rate is much slower than that of the standard Newton-Raphson scheme.

4.3.4 Return-mapping algorithm

The subsection addresses one of the key steps in Newton-Raphson scheme, stress state updating. It relies on the integration algorithms of stress change over the strain path. The adopted

return-mapping method is essentially named as elastic trial and plastic return-mapping method, in which the two steps are employed sequentially. The two steps are explained below:

1. The elastic trial step

It is known that the tangent matrix for the nonlinear elastoplastic model is unknown at the state defined by the displacement. Without knowing the exact value of the elastoplastic tangent matrix $\mathbf{D}^{ep}$, it is assumed that the current incremental step is elastic. So the internal state variables α keep constant, the change in strain is all added to the elastic strain, and $\mathbf{D}^{e}$ is used to predict the stress state. This is called the elastic trial step and is formulated as

$$\alpha_{n+1}^{trial} = \alpha_n \tag{4.43}$$

where α_n is the internal state variable at the last converged increment. So the hardening parameter $\mathbf{k}$ also keeps the same,

$$\mathbf{k}_{n+1}^{trial} = \mathbf{k}_n \tag{4.44}$$

The elastic trial strain is calculated by

$$\boldsymbol{\varepsilon}_{n+1}^{e\,trial} = \boldsymbol{\varepsilon}_{n+1}^{e(k-1)} + \delta\boldsymbol{\varepsilon}^{(k)} \tag{4.45}$$

where $\boldsymbol{\varepsilon}_{n+1}^{e\,trial}$ and $\boldsymbol{\varepsilon}_{n+1}^{e(k-1)}$ is the elastic trial strain for the k^{th} and $(k-1)^{th}$ iteration respectively and $\delta\boldsymbol{\varepsilon}^{(k)}$ is the change of strain calculated by equation(4.29) with $\mathbf{u}$ replaced by $\delta\mathbf{u}^{(k)}$:

$$\delta\boldsymbol{\varepsilon}^{(k)} = \mathbf{B}\delta\mathbf{u}^{(k)} \tag{4.46}$$

Then the stress is updated by equation (4.27) with similar substitution, that is

$$\boldsymbol{\sigma}_{n+1}^{trial} = \mathbf{D}^{e}\boldsymbol{\varepsilon}_{n+1}^{e\,trial} \tag{4.47}$$

or equivalently by applying the deviatoric/volumetric decomposition

$$\mathbf{s}_{n+1}^{trial} = 2G\boldsymbol{\varepsilon}_{d\,n+1}^{e\,trial}, \quad p_{n+1}^{trial} = K\boldsymbol{\varepsilon}_{v\,n+1}^{e\,trial} \tag{4.48}$$

Then the assumption will be checked by the yield function using these trial variables. If

$$\Phi^{trial} \equiv \Phi\left(\boldsymbol{\sigma}_{n+1}^{trial}, \mathbf{k}_{n+1}^{trial}\right) \leq 0, \tag{4.49}$$

which means the trial stress state is within the elastic domain or right on the yield surface, the elastic assumption is accepted and the true solution is just the trial solution and the algorithm moves to the next increment if any. Otherwise, the trial stress state is already out of the region enveloped by the yield surface which is physically inaccessible. In other words, the trial solution is unacceptable and the plastic return step should be executed.

2. The plastic return step

Knowing that the plastic yielding has begun, the stress state is on the yield surface and the plastic straining is also characterized by combining the flow rule and hardening rule. So the plastic return step is essentially solving an equation system defined by the yield condition, the flow rule and the hardening rule which is shown as follows

$$\begin{aligned} &\Phi\left(\boldsymbol{\sigma}_{n+1}, \mathbf{k}_{n+1}\right) = 0 \\ &\boldsymbol{\varepsilon}_{n+1}^{e} = \boldsymbol{\varepsilon}_{n+1}^{e\,trial} - \Lambda \mathbf{N}\left(\boldsymbol{\sigma}_{n+1}, \mathbf{k}_{n+1}\right) \\ &\alpha_{n+1} = \alpha_{n+1}^{trial} - \Lambda \frac{\partial \Phi}{\partial \mathbf{k}}\left(\boldsymbol{\sigma}_{n+1}, \mathbf{k}_{n+1}\right) \end{aligned} \tag{4.50}$$

and the stress state and the hardening parameters are calculated accordingly by

$$\boldsymbol{\sigma}_{n+1} = \boldsymbol{\sigma}_{n+1}^{trial} - \Lambda \mathbf{D}^{e} : \mathbf{N}_{n+1} \tag{4.51}$$

where the material is assumed linear elastic within the elastic domain and $-\Lambda \mathbf{D}^{e} : \mathbf{N}_{n+1}$ as the inner product of these two tensors is the return vector. Then we can conclude that the return-mapping algorithm is basically to find a solution of $\boldsymbol{\varepsilon}_{n+1}^{e}$, α_{n+1} and the plastic multiplier Λ.

The return-mapping is schematically shown in Figure 4-6. The stress state $\boldsymbol{\sigma}_{n}$ is updated by two steps, first the elastic trial step to $\boldsymbol{\sigma}_{n+1}^{trial}$ and second plastic return step to $\boldsymbol{\sigma}_{n+1}$.

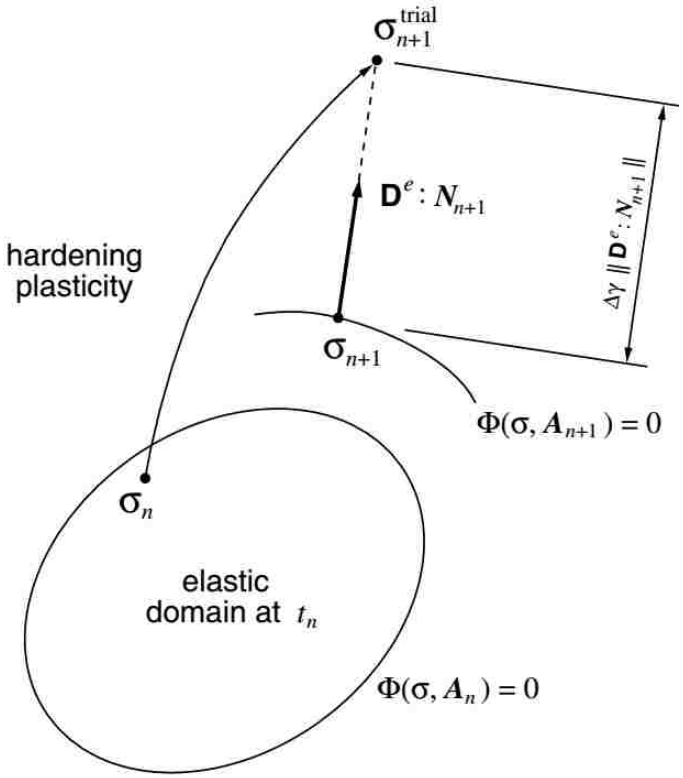

Figure 4-6 Schematic of the implicit return-mapping algorithm for material with linear elasticity and hardening plasticity. Source: "Computational Methods for Plasticity: Theory and Applications," by de Souza Neto et al., 2008, John Wiley & Sons, Ltd, p. 201.

4.4 Returning mapping and consistent tangent for Drucker-Prager model

This section focuses on formulating Drucker-Prager model using the general methodology explained in the above three sections. Two major steps are stress state updating and updating consistent tangent matrix accordingly.

4.4.1 Stress state updating algorithm for Drucker-Prager model

Based on the general return-mapping formula for the stress tensor in equation(4.51)[1], $-\Lambda \mathbf{D}^e : \mathbf{N}_{n+1}$ is the return vector. The return-mapping algorithm for Drucker-Prager model is less complex comparing to Mohr-Coulomb model because of its symmetry about the hydrostatic axis and less singular points involved. As a result of the symmetry, Drucker-Prager yield surface can

be uniquely represented in the $\sqrt{J_2(\mathbf{s})} - p$ plane and the return vector should be parallel to the plane. The return-mapping is schematically shown in such a plane in Figure 4-7. Note that the plotted yield surface is the one after strain hardening.

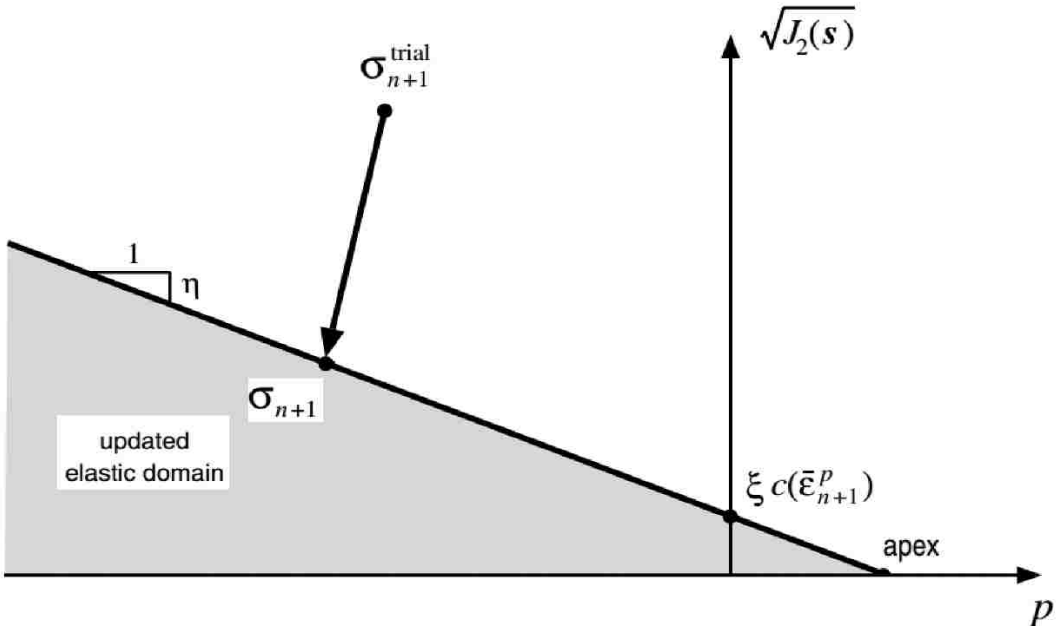

Figure 4-7 Schematic of return-mapping algorithm for Drucker-Prager model. Adapted from: "Computational Methods for Plasticity: Theory and Applications," by de Souza Neto et al., 2008, John Wiley & Sons, Ltd, p. 329.

Explicit formula are derived for the implicit return-mapping algorithm. Note that the plastic flow vector $\mathbf{N}_{n+1}$ are different for the smooth portion and the singular apex of the cone, so two sets of formulas are derived separately.

1. Return to the smooth portion of Drucker-Prager cone

The flow vector on the smooth portion is defined by equation(4.20). Thus the corresponding change of plastic strain is obtained by substituting equation (4.20) into(4.14):

$$\Delta\varepsilon^{p} = \Lambda \boldsymbol{N} = \Lambda\left(\frac{1}{2\sqrt{J_2(\mathbf{s})}}\mathbf{s} + \frac{\bar{\eta}}{3} I\right) \tag{4.52}$$

Using the stress updating equation (4.51)[1], the corresponding stress is updated by

$$\boldsymbol{\sigma}_{n+1} = \boldsymbol{\sigma}_{n+1}^{trial} - \Lambda \mathbf{D}^{e} : \left(\frac{1}{2\sqrt{J_2(\mathbf{s})}} \mathbf{s}_{n+1} + \frac{\bar{\eta}}{3} I \right) \tag{4.53}$$

Or equivalently by applying the deviatoric/volumetric decomposition like equation (4.48)

$$\boldsymbol{\sigma}_{n+1} = \boldsymbol{\sigma}_{n+1}^{trial} - \Lambda \left(\frac{G}{\sqrt{J_2(\mathbf{s})}} \mathbf{s}_{n+1} + \frac{K\bar{\eta}}{3} I \right) \tag{4.54}$$

or separately expressed as

$$\begin{aligned} \mathbf{s}_{n+1} &= \mathbf{s}_{n+1}^{trial} - \frac{G\Lambda}{\sqrt{J_2(\mathbf{s})}} \mathbf{s}_{n+1} \\ p_{n+1} &= p_{n+1}^{trial} - K \mathrm{d}\boldsymbol{\varepsilon}_{v}^{p} = p_{n+1}^{trial} - K\bar{\eta}\Lambda \end{aligned} \tag{4.55}$$

Rearranging the first equation to

$$\left(1 + \frac{G\Lambda}{\sqrt{J_2(\mathbf{s})}} \right) \mathbf{s}_{n+1} = \mathbf{s}_{n+1}^{trial} \tag{4.56}$$

which implies the following important identity

$$\frac{\mathbf{s}_{n+1}}{\left\| \mathbf{s}_{n+1} \right\|} = \frac{\mathbf{s}_{n+1}^{trial}}{\left\| \mathbf{s}_{n+1}^{trial} \right\|} \quad or \quad \frac{\mathbf{s}_{n+1}}{\sqrt{J_2(\mathbf{s}_{n+1})}} = \frac{\mathbf{s}_{n+1}^{trial}}{\sqrt{J_2(\mathbf{s}_{n+1}^{trial})}} \tag{4.57}$$

Substituting the identity to equation (4.55) yields

$$\mathbf{s}_{n+1} = \left(1 - \frac{G\Lambda}{\sqrt{J_2(\mathbf{s}_{n+1}^{trial})}} \right) \mathbf{s}_{n+1}^{trial}; \quad p_{n+1} = p_{n+1}^{trial} - K\bar{\eta}\Lambda \tag{4.58}$$

Note that the above derivation concludes that the updated deviatoric stress $\mathbf{s}_{n+1}$ is simply a function of the trial deviatoric stress $\mathbf{s}_{n+1}^{trial}$ and the plastic multiplier.

Recall the generic stress state updating methodology denoted by equation(4.50), we know the updated stress state should satisfy the yield function, which is

$$\Phi(\sigma, c) = \sqrt{J_2(\mathbf{s}_{n+1})} + \eta p_{n+1} - \xi c\left(\bar{\varepsilon}^p_{n+1}\right) = 0 \tag{4.59}$$

where the updated accumulated plastic strain as the internal hardening variable α is calculated by the discrete equation (4.50)[3]:

$$\bar{\varepsilon}^p_{n+1} = \bar{\varepsilon}^p_n + \xi\Lambda \tag{4.60}$$

Substituting (4.58) and (4.60) into the yield function equation leads to the following equation with only one unknown, the plastic multiplier Λ :

$$\begin{aligned}\hat{\Phi}(\Lambda) \equiv \sqrt{J_2\left(\mathbf{s}^{trial}_{n+1}\right)} - G\Lambda + \eta\left(p^{trial}_{n+1} - K\bar{\eta}\Lambda\right) \\ - \xi c\left(\bar{\varepsilon}^p_n + \xi\Lambda\right) = 0\end{aligned} \tag{4.61}$$

With the solution for Λ, the stress state can be updated by (4.58) and the accumulated plastic strain by equation(4.60). The elastic strain is updated by

$$\boldsymbol{\varepsilon}^e_{n+1} = \frac{1}{2G}\mathbf{s}_{n+1} + \frac{p_{n+1}}{3K} I \tag{4.62}$$

The plastic strain is calculated with the assumption that total strain is the summation of elastic strain and plastic strain, so is the change of total strain:

$$\Delta\varepsilon = \Delta\varepsilon^e + \Delta\varepsilon^p \tag{4.63}$$

All essential formula necessary to return a trial stress state to the smooth section of the cone are already derived in the above. The return-mapping is then checked by the sign of $\sqrt{J_2\left(\mathbf{s}^{trial}_{n+1}\right)} - G\Lambda$, which is the updated $\sqrt{J_2\left(\mathbf{s}_{n+1}\right)}$. If positive, the returned stress state is truly on the smooth portion of the cone and the return-mapping algorithm abort for this iteration. Otherwise, the return-mapping to the apex will be executed. The selection is shown in Figure 4-8.

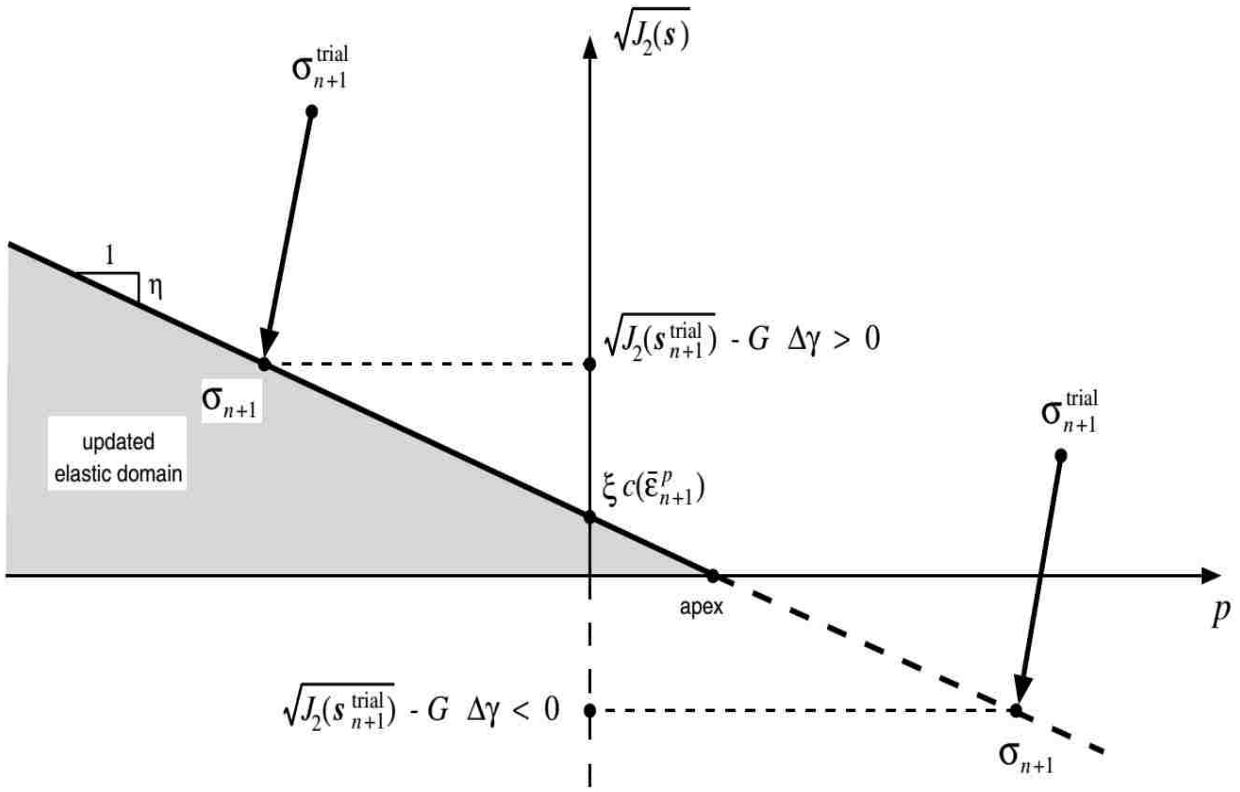

Figure 4-8 Screening of appropriate return-mapping for Drucker-Prager model. Source: "Computational Methods for Plasticity: Theory and Applications," by de Souza Neto et al., 2008, John Wiley & Sons, Ltd, p. 328.

2. Return to the singular apex of the cone

As discussed in section 4.2.2 on page 26, the flow vector must be contained in the complementary cone of Drucker-Prager cone. While the magnitude of deviatoric component is indefinite, the volumetric part is formulated by the non-associative flow rule:

$$\Delta\boldsymbol{\varepsilon}_v^p = \bar{\eta}\Lambda \tag{4.64}$$

Analogous to the smooth portion, the change of accumulated plastic strain is $\xi\Lambda$, so

$$\Delta\bar{\boldsymbol{\varepsilon}}^p = \frac{\xi}{\bar{\eta}}\Delta\boldsymbol{\varepsilon}_v^p \tag{4.65}$$

If the trial stress is returned to the apex, we can ignore the deviatoric component of the return vector because the updated stress has no deviatoric part anymore as geometrically shown in Figure

4-9. Here, we only need return the trial mean stress p_{n+1}^{trial} to the updated apex along the $p-$ axis by $-K\mathrm{d}\boldsymbol{\varepsilon}_v^p \boldsymbol{I}$.

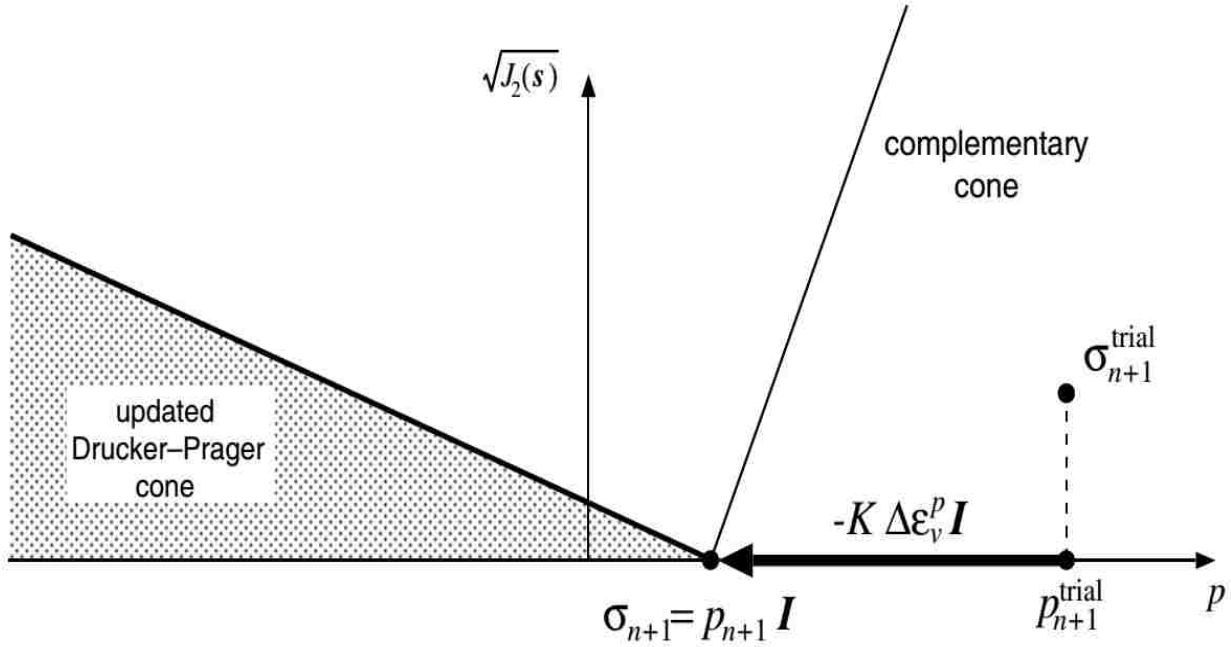

Figure 4-9 Return-mapping to the apex of Drucker-Prager cone. Source: "Computational Methods for Plasticity: Theory and Applications," by de Souza Neto et al., 2008, John Wiley & Sons, Ltd, p. 328.

After ignoring the deviatoric part, the yield function becomes

$$\eta\left(p_{n+1}^{trial}-K\Delta\boldsymbol{\varepsilon}_v^p\right)-\xi c\left(\bar{\varepsilon}_n^p+\Delta\bar{\boldsymbol{\varepsilon}}^p\right)=0 \tag{4.66}$$

The substitution of equation (4.65) reads

$$\hat{\Phi}\left(\Delta\boldsymbol{\varepsilon}_v^p\right)\equiv p_{n+1}^{trial}-K\Delta\boldsymbol{\varepsilon}_v^p-c\left(\bar{\varepsilon}_n^p+\frac{\xi}{\bar{\eta}}\Delta\boldsymbol{\varepsilon}_v^p\right)\frac{\xi}{\eta}=0 \tag{4.67}$$

The yield function then becomes an equation of a single unknown, change of plastic volumetric strain $\Delta\boldsymbol{\varepsilon}_v^p$. The stress state and the internal state variable are updated by

$$\begin{aligned}\boldsymbol{\sigma}_{n+1} &= \left(p_{n+1}^{trial} - K\Delta\boldsymbol{\varepsilon}_v^p \right) I \\ \bar{\varepsilon}_{n+1}^p &= \bar{\varepsilon}_n^p + \frac{\xi}{\bar{\eta}}\Delta\boldsymbol{\varepsilon}_v^p\end{aligned} \tag{4.68}$$

Since $\bar{\eta}$ is the denominator, it cannot be zero. Therefore the above return-mapping algorithm doesn't apply to the non-dilatant flow where $\bar{\eta} = 0$.

If a linear hardening rule is adopted as formulated by equation (4.24), the two yield function for two scenarios, equation (4.61) and equation (4.67) become linear equations and can be solved in closed form. Otherwise, the two equations are solved by standard Newton-Raphson scheme.

4.4.2 Consistent tangent matrix for Drucker-Prager model

Recall the definition of the consistent tangent matrix by equation(4.28):

$$\mathbf{D} \equiv \frac{\partial \boldsymbol{\sigma}}{\partial \boldsymbol{\varepsilon}}$$

The consistent tangent matrix is $\mathbf{D}^e$ within the elastic domain, which is constant in the platform of the linear elasticity. This section is dedicated to the derivation of the elastoplastic tangent matrix $\mathbf{D}^{ep}$ for Drucker-Prager model consistent with the stress state updating algorithm explained above.

In the elastoplastic region, the stress tensor is defined by an incremental constitutive equation as shown in equation (4.34)

$$\boldsymbol{\sigma}_{n+1} = \hat{\boldsymbol{\sigma}}\left(\alpha_n, \boldsymbol{\varepsilon}_{n+1}\right)$$

The substitution into equation (4.28) reads

$$\mathbf{D} \equiv \left.\frac{\partial \hat{\boldsymbol{\sigma}}}{\partial \boldsymbol{\varepsilon}_{n+1}}\right|_{\alpha_n} \tag{4.69}$$

The consistent tangent matrix in the case of Newton-Raphson scheme is the derivative of

algorithmic function $\hat{\boldsymbol{\sigma}}$ with respect to the total strain while α_n keeps constant. For the return-mapping algorithm, the stress tensor is further reduced to a function of elastic trial strain

$$\boldsymbol{\sigma}_{n+1} = \tilde{\boldsymbol{\sigma}}\left(\alpha_n, \boldsymbol{\varepsilon}_{n+1}^{e\,trial}\right) \equiv \hat{\boldsymbol{\sigma}}\left(\alpha_n, \boldsymbol{\varepsilon}_{n+1}\right) \tag{4.70}$$

where, $\boldsymbol{\varepsilon}_{n+1}^{e\,trial} = \boldsymbol{\varepsilon}_{n+1} - \boldsymbol{\varepsilon}_n^p$ and $\tilde{\boldsymbol{\sigma}}$ is the stress updated by the return-mapping algorithm. We also have the following identity

$$\mathbf{D} \equiv \left.\frac{\partial \hat{\boldsymbol{\sigma}}}{\partial \boldsymbol{\varepsilon}_{n+1}}\right|_{\alpha_n} = \left.\frac{\partial \tilde{\boldsymbol{\sigma}}}{\partial \boldsymbol{\varepsilon}_{n+1}^{e\,trial}}\right|_{\alpha_n} \tag{4.71}$$

Considering that the yield functions (4.61) and (4.67) are formulated in terms of elastic trial stress, we select the rightmost term of the above equation for the ease of formulation.

As is in the stress state updating algorithm, the consistent tangent matrix will have two forms for the smooth portion and the apex respectively.

1. Tangent matrix consistent with return-mapping to the smooth portion

Recall the updated stress through return-mapping to the smooth portion by equation(4.58). First, the trial deviatoric stress is expressed in terms of the trial deviatoric strain by means of the constitutive equations and the definition of J_2 invariant, that is

$$\mathbf{s}_{n+1} = \left(1 - \frac{G\Lambda}{\sqrt{J_2\left(\mathbf{s}_{n+1}^{trial}\right)}}\right)\mathbf{s}_{n+1}^{trial} = 2G\left(1 - \frac{\Lambda}{\sqrt{2}\left\|\boldsymbol{\varepsilon}_{d\,n+1}^{e\,trial}\right\|}\right)\boldsymbol{\varepsilon}_{d\,n+1}^{e\,trial} \tag{4.72}$$

So the differential of the deviatoric stress with respect to the trial elastic deviatoric strain gives

$$\mathrm{d}\mathbf{s}_{n+1} = 2G\left[\left(1 - \frac{\Lambda}{\sqrt{2}\left\|\boldsymbol{\varepsilon}_{d\,n+1}^{e\,trial}\right\|}\right)\mathrm{d}\boldsymbol{\varepsilon}_{d\,n+1}^{e\,trial} + \frac{\Lambda}{\sqrt{2}\left\|\boldsymbol{\varepsilon}_{d\,n+1}^{e\,trial}\right\|} D \otimes D : \mathrm{d}\boldsymbol{\varepsilon}_{d\,n+1}^{e\,trial} - \frac{1}{\sqrt{2}}\mathrm{d}\Lambda D\right] \tag{4.73}$$

where the symbol $\otimes$ stands for the tensor product of tensors, and the second-order tensor D is the unit tensor parallel to $\boldsymbol{\varepsilon}_{d\,n+1}^{e\,trial}$:

$$D = \frac{\boldsymbol{\varepsilon}_{d\,n+1}^{e\,trial}}{\left\| \boldsymbol{\varepsilon}_{d\,n+1}^{e\,trial} \right\|} \tag{4.74}$$

Also note that the plastic multiplier is an implicit function of $\boldsymbol{\varepsilon}_{d\,n+1}^{e\,trial}$, so the differentiation must take account for $\mathrm{d}\Lambda$ as well. By the similar procedure, the mean stress component of the updated stress tensor reads

$$p_{n+1} = p_{n+1}^{trial} - K\bar{\eta}\Lambda = K\left(\boldsymbol{\varepsilon}_{v\,n+1}^{e\,trial} - \bar{\eta}\Lambda\right) \tag{4.75}$$

And the differentiation yields

$$\mathrm{d}p_{n+1} = K\left(\mathrm{d}\boldsymbol{\varepsilon}_{v\,n+1}^{e\,trial} - \bar{\eta}\,\mathrm{d}\Lambda\right) \tag{4.76}$$

Now the differentials of the trial strains and the plastic multiplier are related via the substitution of the yield function (4.61) for the return-mapping into consistency condition(4.2):

$$\begin{aligned} \mathrm{d}\hat{\Phi}\left(\Lambda\right) = \sqrt{2}GD : \mathrm{d}\boldsymbol{\varepsilon}_{d\,n+1}^{e\,trial} + K\eta\,\mathrm{d}\boldsymbol{\varepsilon}_{v\,n+1}^{e\,trial} \\ -\left(G + K\eta\bar{\eta} + \xi^2 H\right)\mathrm{d}\Lambda = 0 \end{aligned} \tag{4.77}$$

$$\mathrm{d}\Lambda = \frac{1}{G + K\eta\bar{\eta} + \xi^2 H}\left(\sqrt{2}GD : \mathrm{d}\boldsymbol{\varepsilon}_{d\,n+1}^{e\,trial} + K\eta\,\mathrm{d}\boldsymbol{\varepsilon}_{v\,n+1}^{e\,trial}\right) \tag{4.78}$$

Now the identity for the consistent tangent matrix is introduced, so

$$\mathbf{D}^{ep} \equiv \frac{\partial\tilde{\boldsymbol{\sigma}}}{\partial\boldsymbol{\varepsilon}_{n+1}^{e\,trial}} = \frac{\partial\mathbf{s}_{n+1}}{\partial\boldsymbol{\varepsilon}_{n+1}^{e\,trial}} + I \otimes \frac{\partial p_{n+1}}{\partial\boldsymbol{\varepsilon}_{n+1}^{e\,trial}} \tag{4.79}$$

Substituting equation(4.73), (4.76) and (4.78) into the above identity gives the explicit expression of the elastoplastic tangent matrix. After some manipulation, the matrix reads

$$\begin{aligned} \mathbf{D}^{ep} = 2G\left(1 - \frac{\Lambda}{\sqrt{2}\left\|\boldsymbol{\varepsilon}_{d\,n+1}^{e\,trial}\right\|}\right)\mathrm{I}_d + 2G\left(\frac{\Lambda}{\sqrt{2}\left\|\boldsymbol{\varepsilon}_{d\,n+1}^{e\,trial}\right\|} - GA\right)D \otimes D \\ -\sqrt{2}GAK\left(\eta D \otimes I + \bar{\eta}\,I \otimes D\right) + K\left(1 - K\eta\bar{\eta}A\right)I \otimes I \end{aligned} \tag{4.80}$$

where I_d is the fourth-order deviatoric projection tensor and A is

$$A = \frac{1}{G + K\eta\bar{\eta} + \xi^2 H} \tag{4.81}$$

2. Tangent matrix consistent with return-mapping to the singular apex of the cone

By similar technique used for the smooth portion, the tangent matrix consistent with the return-mapping to the apex is derived here with added simplicity since only the volumetric component needs to be addressed. So equation (4.79) is reduced to

$$\mathbf{D}^{ep} \equiv I \otimes \frac{\partial p_{n+1}}{\partial \boldsymbol{\varepsilon}_{n+1}^{e\,trial}} \tag{4.82}$$

Recall the mean stress updating equation:

$$p_{n+1} = p_{n+1}^{trial} - K\Delta\boldsymbol{\varepsilon}_v^p \tag{4.83}$$

The differentiation is

$$\mathrm{d}p_{n+1} = K\left(I : \mathrm{d}\boldsymbol{\varepsilon}_{v\,n+1}^{e\,trial} - \mathrm{d}\Delta\boldsymbol{\varepsilon}_v^p\right) \tag{4.84}$$

The consistency condition for the apex is

$$\mathrm{d}\hat{\Phi}\left(\Delta\boldsymbol{\varepsilon}_v^p\right) = KI : \mathrm{d}\boldsymbol{\varepsilon}_{v\,n+1}^{e\,trial} - K\mathrm{d}\Delta\boldsymbol{\varepsilon}_v^p - \frac{\xi}{\eta}\frac{\xi}{\bar{\eta}} H\mathrm{d}\Delta\boldsymbol{\varepsilon}_v^p = 0 \tag{4.85}$$

Therefore, the differential $\mathrm{d}\Delta\boldsymbol{\varepsilon}_v^p$ can be expressed as

$$\mathrm{d}\Delta\boldsymbol{\varepsilon}_v^p = \frac{K}{K + \frac{\xi}{\eta}\frac{\xi}{\bar{\eta}} H} I : \mathrm{d}\boldsymbol{\varepsilon}_{v\,n+1}^{e\,trial} \tag{4.86}$$

After the substitution of the above equation and (4.84) into(4.82), the consistent tangent matrix for the return-mapping to the apex is expressed as

$$\mathbf{D}^{ep} = K\left(1 - \frac{K}{K + \frac{\xi}{\eta}\frac{\xi}{\bar{\eta}} H}\right) I \otimes I \tag{4.87}$$

It is interesting to note that this consistent tangent matrix is constant for linear hardening model since H is a constant material parameter. Also one can observe that the above equation vanishes for the perfect plasticity model where the hardening parameter is constantly 0. In other words, the stress state is fixed to the apex for perfect plasticity model.

The theoretical methods used in this thesis project have been addressed in this chapter. As mentioned in the beginning of the chapter, more details about the fundamental theory and the formulation of other elastoplastic models can be found in the works by David, M. Potts and de Souza Neto et al.

Chapter 5 Overview of the Program Structure

The above chapter was focused on the theoretical strategy for the finite element analysis of the nonlinear solid mechanics. Specifically, all necessary formulation have been derived for Drucker-Prager model. As mentioned above, the thesis project is aimed at numerically simulating the deformation, the plastic straining and stress evolution for wellbore stability problems. The numerical simulation is carried out on the platform, NSMOOM, which is short for Nonlinear Solid Mechanics in Object-oriented MATLAB. This platform built for the thesis is not only capable to solve the wellbore stability problem; it is but also a well-constructed finite element analysis environment which can be easily set up for different problems with various geometry, boundary conditions and material properties. Various material models can be incorporated by adding only one descendant class of "GaussPnt" class. Even though this platform is only armed with the linear elastic model and Drucker-Prager model, the platform has the potential to do various geomechanics analysis in petroleum engineering, like sanding, reservoir compaction, etc.

This section will provide an overall description of NSMOOM platform with the emphasis on the structure in that it is not practical to explain everything for the program in the thesis. A brief introduction of object-oriented language is presented first. Then the structure of the whole platform will be provided by addressing the relationship between every module. Finally, a flow chart will be provided to show how the fore-mentioned algorithms in Chapter 4 work in the NSMOOM.

5.1 An introduction to object-oriented programming

Object-oriented programming is not simply a programming language. Instead, it is a relatively new programming philosophy which fundamentally differs from the classical procedural programming. In object-oriented programming, the data and the associated functions are built together, which is called encapsulation. Whereas, the data and functions in the procedural

programming are linked to each other only when the functions are called (Mackie, 1992). This comparison is schematically shown in Figure 5-1.

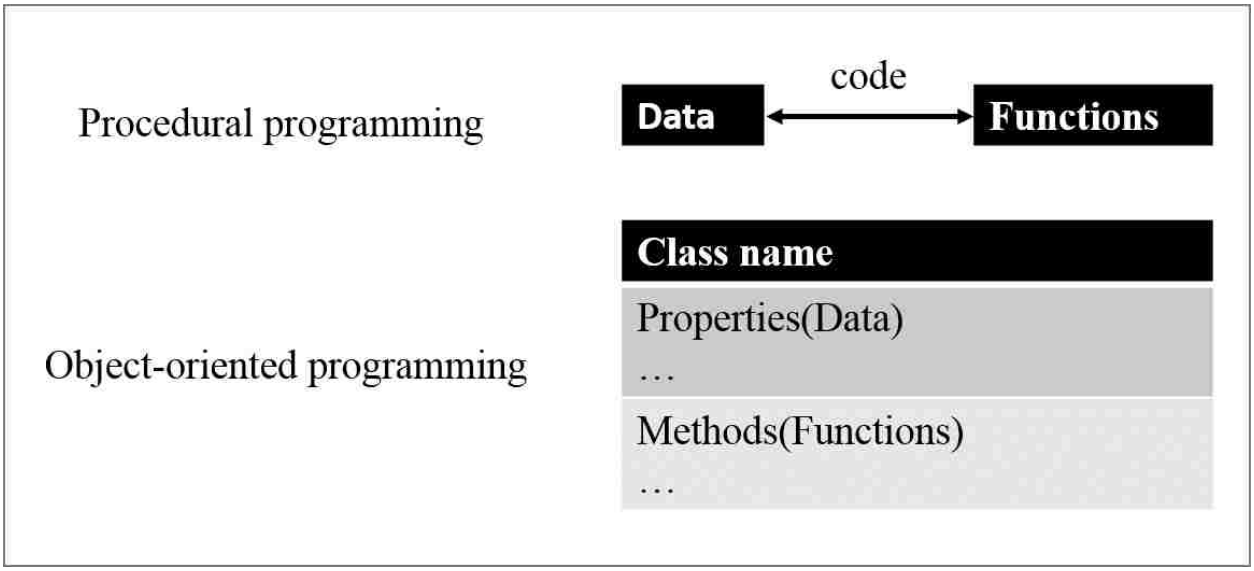

Figure 5-1 Comparison on the data-function relationship

Many new terminologies for the object-oriented programming are introduced. The most important concepts are "class" and "object". An object is an instance of a class. Generally speaking, a class abstractly lists the common properties and concretely defines methods of a group of entities, while an object as an instance has concrete value for the properties and can execute the methods defined by the class.

Classes are the basis of object-oriented programming. A class must be defined before an object of this class can be instantiated. The definition of a class consists two parts: properties and methods, as shown in Figure 5-1. Properties define what kind of information this class owns and methods describe what behaviors the class can have. Properties and the methods are encapsulated which means those methods can only be called by the objects of this class. This is the difference between methods and standard functions in the procedural programming. Due to the definition of

class, the data are automatically stored in a structured manner after computation. The advantage of structured data management is even amplified when the hierarchical classes are well defined.

Inheritance is another landmark of object-oriented programming, which has been used and argued extensively by the programmers. This feature enables programmers to define a new class which can inherit all properties and methods from an existing class. In this way, the old program can be maintained and updated much more efficiently. However, as mentioned above, the feature of inheritance is not universally good for programming. The right use of inheritance will greatly increase the reusability and augmentability of the developed code. However, the code can become chaotic if the inheritance feature is employed blindly. NSMOOM was developed carefully to avoid the disadvantage of inheritance.

Another extensively used technique in NSMOOM is the abstract class. Different from the standard class, the abstract class only announces the name of the methods without programming certain codes to make the method executive. These methods are also referred to abstract methods. Objects cannot be instantiated from an abstract class. Then standard classes will be derived from the abstract class to fulfill all abstract methods. Note that if the descendant class doesn't define all abstract methods, it is still an abstract class. The reason to define an abstract class is to make the program more modular. The abstract class can be used as an interface between modules. The other module can call this interface by just knowing the name of the abstract methods without considering what descendant class is used. Inside the module, there can be multiple ways to define these abstract methods in multiple descendant classes. But these classes don't need worry about how the other modules will interact with them because the interface is already defined. This feature is also known as the polymorphism.

In summary, the object-oriented programming is beneficial to the finite element method because: 1. its hierarchical structure is very suitable for the hierarchy of the finite element method; 2. the inheritance feature and abstract class feature accommodate the flexibility and augmentability of the finite element analysis code; 3. the self-explanatory feature and the automatic storage management make the finite element analysis program well documented.

5.2 The structure of the program

There are many programming languages supporting object-oriented programming such as C++ and Turbo Pascal. NSMOOM in this project is developed in the object-oriented MATLAB environment because MATLAB has a powerful library to support engineering computation.

The finite element analysis follows such a fixed procedure: preprocessing, computing, and post-processing. This fixed procedure indicates the modularity of the algorithm. Note that the object-oriented programming is by its nature modular. So the structure of the program in object-oriented language will be very analogous to that of the finite element algorithm. Also note that finite element method has a specific calculation order. It always starts the calculation from the basic level and then assemble to the higher level. Specifically, the method attaches the primary unknowns or degree of freedom to the discrete nodes. The nodes then make up of elements and those elements are assembled to make up a whole domain.

Based on the structure of the finite element analysis and internal hierarchy of finite element method, NSMOOM mainly consists of three packages: “ToolPack”, “FEPack” and “DomainPack”. As shown in Figure 5-2, ToolPack as the external assisting facility for the finite element analysis is mainly made up of the “Preprocessor” class and the “Postprocessor” class. FEPack and DomainPack are respectively the elemental level and the global level of the finite element method for computing. The FEPack generally consists of the “Elem”, the “Node” and the “GaussPnt”

classes. One can also see the hierarchy within one package. The DomainPack mainly contains the "Domain class" as the center controlling class, the "NewRapItr" class as the director for the nonlinear iterative algorithm and the "LinSysCreater" class as the director of building the linear equation system for the finite element method.

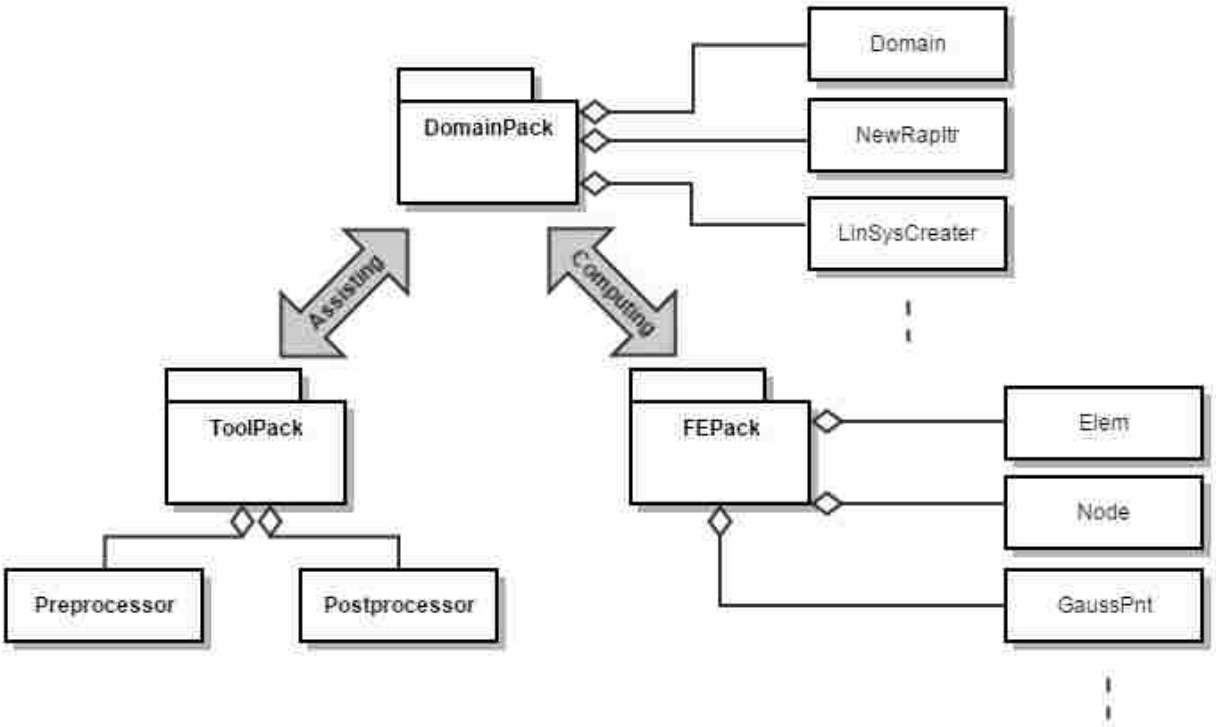

Figure 5-2 Overall physical structure of the NSMOOM program

The logical relationship between each class is the very important to understand a numerical program. The class diagram is illustrated in Figure 5-3 to show the logical structure and the responsibilities of each class. This figure generally follows the convention of the unified modeling language, where a box denotes a class. There are generally three blocks in a box, containing the name, properties and methods of the class. A white arrow stands for inheritance; a while diamond arrow is for aggregation relationship and a solid arrow represents composition relationship.

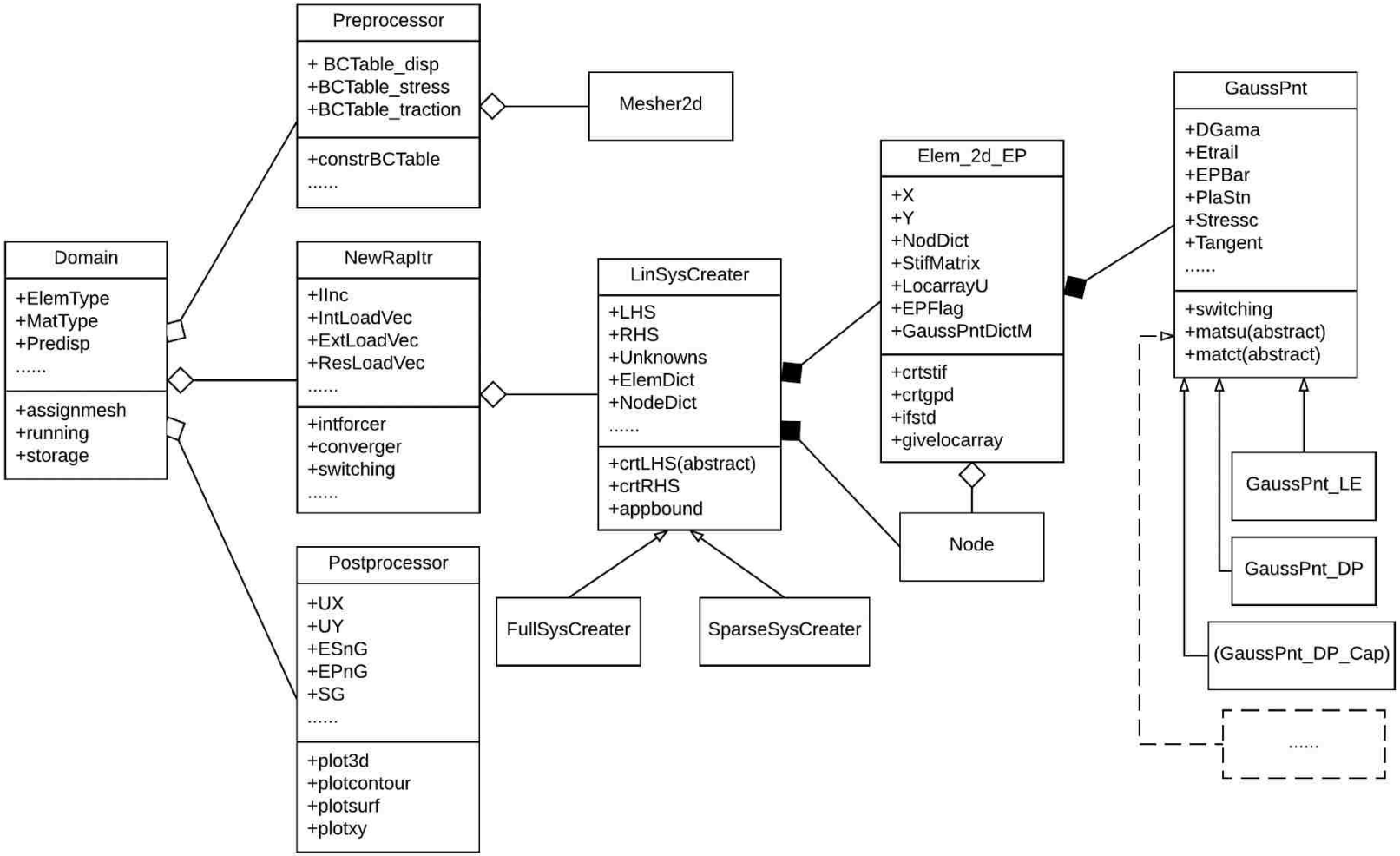

Figure 5-3 Class diagram of NSMOOM in Unified Modeling Language

To explain the class diagram, the design pattern must be discussed first. NSMOOM employs the “Builder” design pattern in object-oriented programming extensively. This pattern is made up of the administrative “director”, “abstract builder” and “concrete builder”. The director is on the highest hierarchy and the concrete builder is on the lowest level. The abstract class becomes an interface between them. While the director stipulates the procedures by integrating abstract builders, the concrete builders execute each step.

The object-oriented programming philosophy encourages the decentralization of the function of each class. And the “Builder” design pattern offers a method to call and control the decentralized class within one class. In a complex program like NSMOOM, the design pattern can be mixed or repeated through the hierarchical structure. See Figure 5-3, the builder pattern can be observed everywhere. On the left part of the diagram, the builder pattern achieves the control over three major procedure of finite element analysis within one single class, “Domain”. In NSMOOM, the Domain class is the overall director of the finite element analysis. It mainly integrates “Preprocessor” class, “NewRaphItr” class and “Postprocess” class which are corresponding to the three procedures of the nonlinear finite element analysis. These three classes are standard classes and the abstractions are delegated to lower levels when various ways of execution are required. For example, there are different ways to store the linear equation system in MATLAB, either full matrix form or sparse matrix form. Thus the “LinSysCreater” class is defined as an abstract class and “FullSysCreater” and “SparseSysCreater” are defined to construct full matrix form and sparse matrix form respectively.

On the rightmost part, another builder pattern has more critical meaning for the code development of elastoplastic solution in object-oriented programming. The “Elem_2d_EP” class as the core of the finite element method is the director here. As we all know, the Gaussian

integration point class are the real builders for the finite elements. Also, the behavior of the Gaussian integration points varies for different materials. Thus the "GaussPnt" class is set as an abstract class and concrete builder classes for different materials are derived from the abstract class. NSMOOM has built the "GaussPnt_LE" for the linear elastic material and "GaussPnt_DP" for Drucker-Prager model. The formulation for a modified Drucker-Prager Cap model is finished but the programming work hasn't been done. It is emphasized that the NSMOOM is open for extension in that only a single GaussPnt descendant class is required to enable NSMOOM solve a new elastoplastic material, as long as one can develop the return-mapping algorithm for the material. Fortunately, the formulation work has been published for most classical elastoplastic models, like the multi-surface Mohr-Coulomb model and the advanced Modified Cam Clay model, etc.

Note that the aggregation and composition relationship are dominant while the inheritance is limited in the class diagram. This corresponds to the fore-mentioned principle to avoid the blind use of inheritance.

Another advantage to take the hierarchical design is that the data storage is automatically structured. The data for each Gaussian points can be retrieved all the way from the Domain class on the highest hierarchy. A lot of time and effort can be saved from defining a well-designed data storing system separately in the procedural programming.

5.3 The flow chart of the computation module

Known the philosophy of object-oriented programming and the logical structure of the program, the flow chart of the main algorithm is described in this subsection. In NSMOOM, it is the "running" method in the "Domain" class. The method is represented by the flow chart in Figure 5-4. The pre-process and post-process procedures are not included in the "running" method as they are not part of the computing module as shown in Figure 5-2.

The running method of Domain class has control over the three major procedures. Once the model is set up, the calculation can be controlled in this single method. The first step is to calculate the global external force vector which is called "FullExtLoad" in the NewRapItr class. Note that the FullExtLoad is only calculated for once because the proportional loading is assumed in the program. Proportional loading means the loading is proportionally cut into several steps. For each step, the ratio between every load component is fixed, i.e., the loading path is a straight line. Mathematically, the proportional loading entails the following equations

$$\begin{aligned} \mathbf{b}_{n+1} &= \lambda_{n+1}\mathbf{b}_{\text{full}} \\ \mathbf{t}_{n+1} &= \lambda_{n+1}\mathbf{t}_{\text{full}} \end{aligned} \tag{4.88}$$

where $\mathbf{b}_{\text{full}}$ and $\mathbf{t}_{\text{full}}$ are the predefined full body force and the traction force; and $\mathbf{b}_{n+1}$, $\mathbf{t}_{n+1}$ are the incremental load controlled by the accumulative increment ratio λ_{n+1} at the $(n+1)^{th}$ increment. Note that the full external load is constant over the calculation procedure, so the computed FullExtLoad is also a constant vector. As a result, the FullExtLoad $\mathbf{f}_{\text{full}}^{\text{ext}}$ is only calculated once and the incremental external force vector $\mathbf{f}_{n+1}^{\text{ext}}$ is obtained by

$$\mathbf{f}_{n+1}^{\text{ext}} = \lambda_{n+1}\mathbf{f}_{\text{full}}^{\text{ext}} \tag{4.89}$$

How the results are stored is set by the "save mode" in the external main script where users set up and control NSMOOM. Save mode is basically a setting to prescribe how often the results are saved. By default, the result after each increment is saved to a Postprocessor object. If too many increments are involved, one can save the converged results every several increments. A Postprocessor object is preallocated for each increment to be saved.

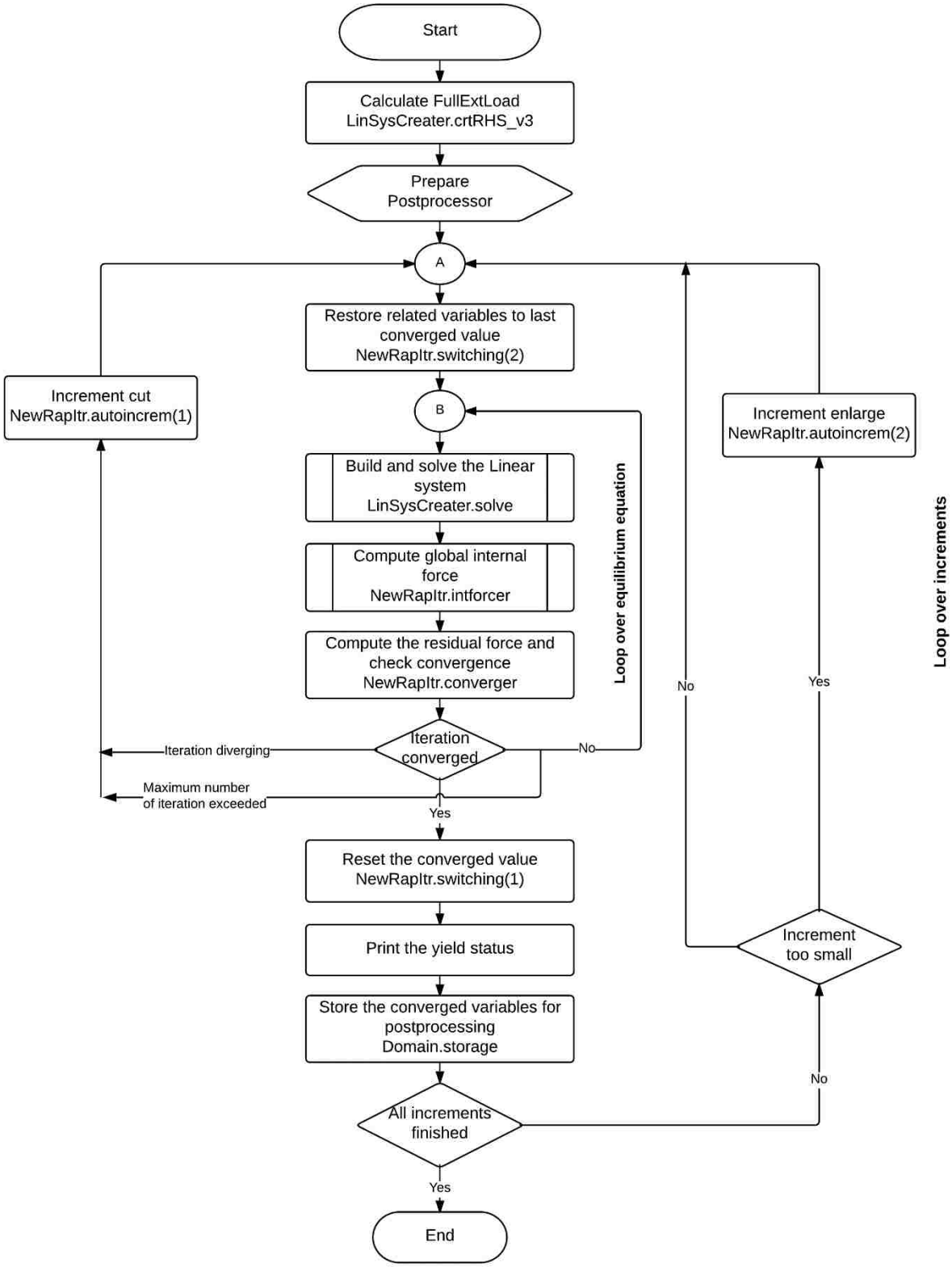

Figure 5-4 Flowchart of the algorithm in the computation module

One can easily observe that a double-loop is the majority of the flowchart. The external loop goes over all incremental steps starting from circle A in Figure 5-4. The internal loop implements the Newton-Raphson algorithm from circle B.

The external loop starts from restoring related variables to the state at the end of the last converged step. This step is critical for the incremental solution of a nonlinear problem as it can assure that every new increment continues from the last converged state. For the first increment step, the last converged state is the prescribed initial state. The details about what parameters are restored is referred to the "switching" method of NewRapItr class.

Once the restoration is finished, the iterative solver over one increment begins. In Figure 5-4, the first step is to build and solve the linear equation system by calling the "solve" method of the LinSysCreater class. The right-hand-side of the linear system for the first iteration is straightforward given by the calculated FullExtLoad. The left-hand-side, also known as the global stiffness matrix is constructed by the descendant class of the LinSysCreater. The SparseSysCreater is preferred since it takes less storage space which is especially necessary for a meshed domain with a great number of nodes. The global stiffness matrix is assembled from element stiffness matrix constructed by every "Elem_2d_EP" object. The nodal displacements are solved from the linear equation system. According to Newton-Raphson algorithm, the internal force vector should be calculated as shown in equation(4.36). This step is predefined by the "intforcer" method of the NewRapItr class. By the philosophy of the finite element method, the variables of the higher hierarchy are always assembled from those on the lower levels. One should note that the stress updating algorithm is implemented on the lowest level, the Gaussian integration points. See Figure 5-3, the stress updating method is called "matsu" of the "GaussPnt" class. This method takes in the updated strain tensor and gives out the updated stress tensor at the gauss point by using the

return-mapping algorithm. The stress tensors at Gaussian points within one element are then used to evaluate the force vector over the element. Finally, the element force vectors are assembled by the intforcer method to give the global internal force vector.

Given the global internal force vector, the residual force vector is computed by equation(4.40). If the residual force vector is close to zero, the iteration is called converged. In NSMOOM, the convergence criterion defined in the "converger" method of NewRapItr class in Figure 5-4 sets a tolerance for the concept of the relative error. The mathematical form is expressed by

$$ratio \equiv \frac{\left\| \mathbf{r}\left(\mathbf{u}_{n+1}\right) \right\|}{\left\| \mathbf{f}_{n+1}^{\text{ext}} \right\|} < tol \tag{4.90}$$

where $\|(\cdot)\|$ is Euclidean norm and the *ratio* is the defined the relative error; *tol* is the defined tolerance. If the above inequality is satisfied, the iteration over the equilibrium equation is converged. In NSMOOM, the property setting of the Newton-Raphson algorithm, including the tolerance, maximum iteration number and maximum number of increments, can be modified by user. By default, the tolerance is set to 10^{-6} considering both the speed of convergence and the accuracy of the iterative method. If convergence is not satisfied, the situation becomes more complicated. One can observe that two more flow lines are pointing to an external procedure "autoincrem (1)" to cut the increment size. The increment cut procedure is activated when either the iteration is diverging (the residual is not decreasing but increasing gradually) or the iteration number has exceeded the predefined maximum number. Note that after increment cut procedure, the program has to be restored to the last converged increment. Normally, the convergence can be obtained after one or two increment cut procedures. However, if the cut procedure has been called

several times and the convergence criterion is still not satisfied, NSMOOM will abort computation. One potential error can be that the size of the initial increment is too large.

The loop over the equilibrium equation for the current increment ends upon the convergence. But there are several procedures before moving to the next the increment step. First, the converged results, like displacement, strain and stress are stored. This is done by the same method as the one to restore values from last converged state, with a different operation mode. It is called by "switching (1)" as shown in Figure 5-4. Second, the status of the current increment step is printed in the screen notifying the yield status, and after how many iterations the equilibrium equation is converged. Third, specific results related to the post-process procedure are stored to the predefined Postprocessor object by calling the "storage" method of Domain class. There is another check point for the increment size before moving on. NSMOOM can automatically adjust the size of following increments based on the performance of the current increment. If the equilibrium equation is converged within only one or two iteration and the increment cut procedure has not been activated for this increment, it is obvious that the current size increment is too small. It is a waste of time and computation resource if the size is not changed. Using the same method to cut increment by different mode, the increments later on are enlarged by "autoincrem (2)." Note that the decision to enlarge the increment size should be made very carefully. If the condition is set too loose or the enlargement is too big, one can expect a significant error or trouble in getting convergence for elastoplastic material. Finally, the algorithm can go to the next increment step. This loop over the increments finishes when all the increments have been computed.

In this subsection, the flowchart of the main method of NSMOOM is explained step by step. The main method belongs to Domain class which is located on the highest hierarchy of the program. So all the procedures are directly done by the classes in the DomainPack. However, one should

note that the detailed calculation are executed in the lower level as discussed before. This is the philosophy of finite element method. The fact that the hierarchical structure of the finite element method takes full advantage of the object-oriented programming which is by nature modular is confirmed at this point. As mentioned above, another advantage is that the data storage is automatically organized in the same hierarchical structure. This feature is very important since data on the lowest level can be queried from the highest level.

5.4 Highlights of NSMOOM

1. The program is completely written in the most popular technical computing package MATLAB. In other word, the simulator can assist many graduate students and engineers in using and understanding any finite element analysis software.
2. The self-explanatory feature and the automatic storage management make the finite element analysis program well documented.
3. NSMOOM is open for extension. Only a single "GaussPnt" descendant class is required to enable NSMOOM to solve a new elastoplastic model.
4. The simulator is built modular. Adding or modifying a single module would not affect the other modules as long as the interface between modules maintains. So different mesh generator can be plugged in this simulator. And the results can be directly exported to other post-processor without any complexity.
5. The simulator supports the multiple boundary conditions. Zero displacement, nonzero displacement and stress condition can all be set.
6. NSMOOM also supports different kinds of loading conditions including concentrated nodal loads, pressure loads and distributing traction force.

Chapter 6 The Preliminary Verification

NSMOOM has been explained briefly in the above chapter. However, the correctness of a program must be verified before being applied to real cases. NSMOOM can handle both pure elastic and elastoplastic material. Note that rigid analytical solutions of the elastoplastic model for anisotropic wellbore problem is still not available. However, the analytical solution of the elastic model which is initially developed by Bradley has been popular through the drilling industry for several decades. This analytical solution of the elastic model is used to do the preliminary verification.

6.1 Setup the numerical model

The wellbore drilling problem is analyzed in two steps. In the first step, initial conditions and boundary conditions are assigned but no deformation is allowed after the removal of rock during drilling. In the second step, the loads condition is applied and the deformation is analyzed.

For the first step, the geometry, initial condition and essential boundary conditions of the wellbore problem are provided below in Figure 6-1. Assuming the double symmetry of the problem, only a quarter of the domain is extracted to reduce the simulation cost and to get rid of the possibility of rigid motion. The current mesh gives a $40*18$ element domain. The mesh is finer near the internal boundary to improve the accuracy of numerical simulation, but the mesh size increases when it approaches to the external boundary where coarse mesh is sufficient because stress remains almost constant.

The stress state over the domain is in-situ stress. As stated before, the minimum horizontal stress is parallel to the x-direction and the overburden stress is applied in the y-direction. Attention should be given to the two symmetry boundaries along x- and y-axis to establish the kinematic

boundary conditions. According to Zervos et al., the essential boundary conditions are constraining $u_y = 0$ along x axis and $u_x = 0$ along y axis (Zervos et al., 2001).

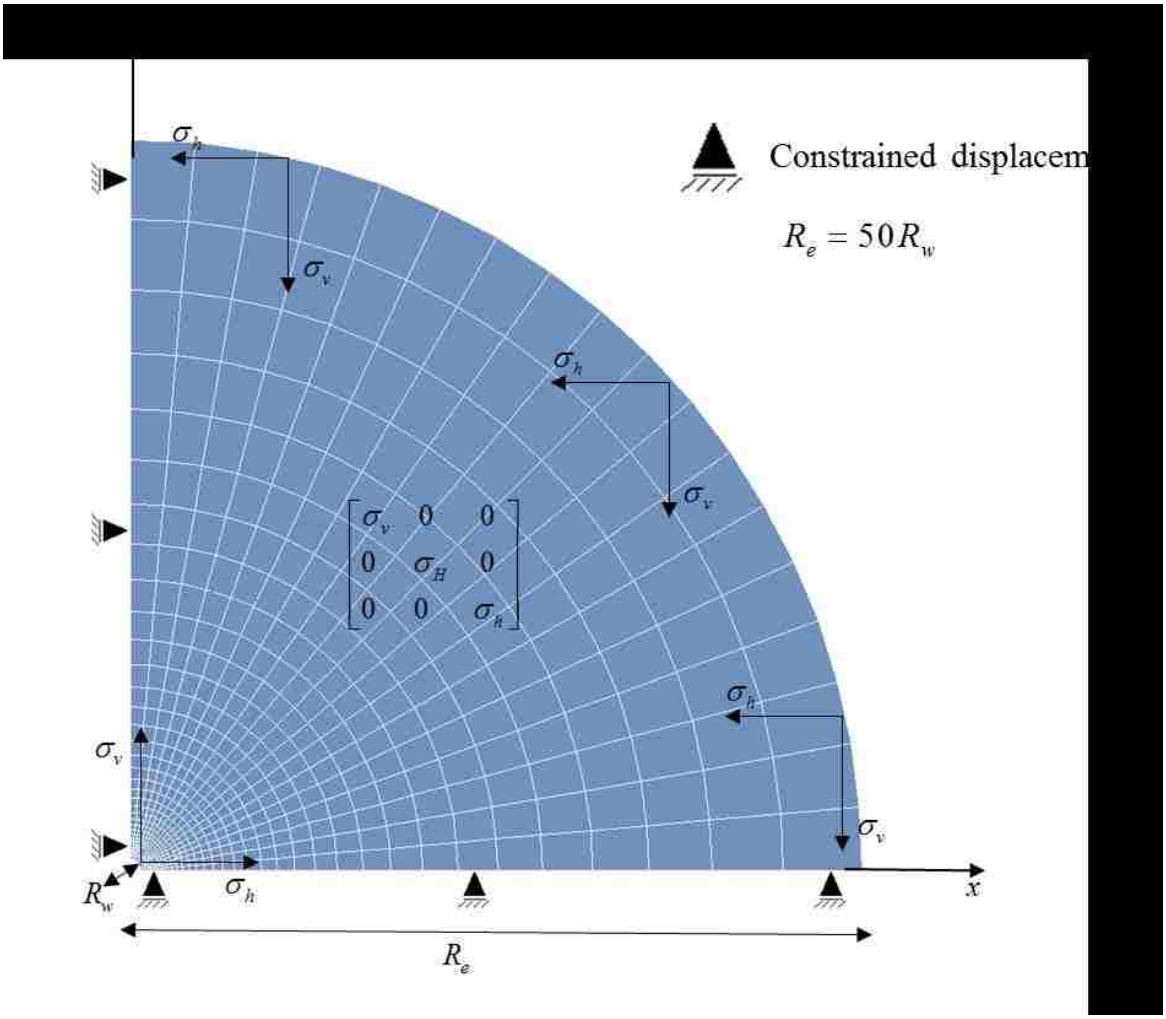

Figure 6-1 Geometry, initial condition and boundary condition of a wellbore domain

In the second step, the domain starts to deform due to the loss of support. See Figure 6-2, the wellbore pressure p_w is applied to the borehole surface. The loads to the external boundary , the in-situ stress, are not disturbed. Because the ratio of the external reservoir radius to the internal wellbore radius, 50:1, is high. The essential boundary conditions for the two axes remain the same as defined.

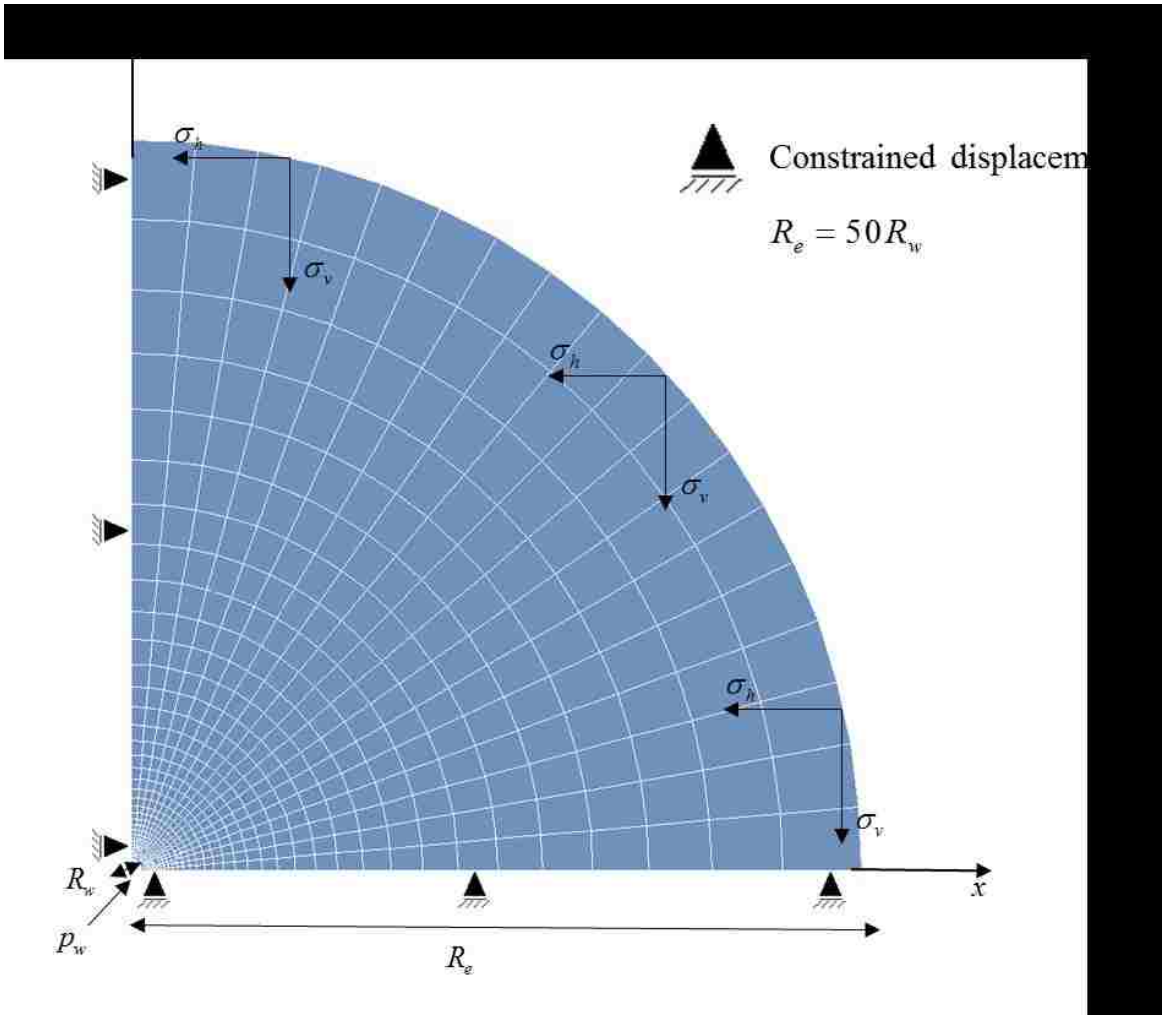

Figure 6-2 Geometry, loads and boundary condition in the second step

Next step is to retrieve material data and stress data. Reported data of Berea sandstone in the Gulf Coast by Morita and Gray is used for the current validation. Note the convention here is that tensile stress as positive stress. At 10,000 ft, for the conditions reported, minimum horizontal stress is -7.37 $kpsi$, maximum horizontal stress is -8.48 $kpsi$, and the overburden stress is -10 $kpsi$. The pore pressure estimated from the pore pressure gradient is 4.35 $kpsi$. The Young's modulus, Poisson's ratio and tensile strength approach approximately 3.7×10^3 $kpsi$, 0.14 and 0.2 $kpsi$. Assume the internal friction angle is 20° and thus the cohesion is estimated as 72.8 psi based on

the tensile strength and internal friction angle. All the material parameters are summarized in Table 6-1 in both SI and field units.

Table 6-1 Input parameters for verification problem

Parameters	Field	SI
Young's modulus, E	$3.7\times10^{3}\,kpsi$	$2.55\times10^{4}\,MPa$
Poisson's ratio, ν	0.14	0.14
Overburden stress, σ_v	$-10\,kpsi$	$-68.95\,MPa$
Maximum horizontal stress, σ_H	$-8.48\,kpsi$	$-58.47\,MPa$
Minimum horizontal stress, σ_h	$-7.37\,kpsi$	$-50.81\,MPa$
Initial pore pressure, p_{pi}	$4.35\,kpsi$	$30\,MPa$
Wellbore pressure, p_w	$5.93\,kpsi$	$40.9\,MPa$
Wellbore radius, R_w	$3.94\,in$	$0.1\,m$
Reservoir radius, R_e	$16.40\ ft$	$5\,m$

6.2 The analytical solution

The analytical solution extensively used in the petroleum industry exists for the linear elastic constitutive model. This solution was first used in cylindrical coordinate system for inclined wells by petroleum engineers (W. B. Bradley, 1979). The solution for total stress is correct for both dry rock condition and fully drained condition. For our 2D verification problem, where the wellbore is aligned with the maximum horizontal stress, thus

$$\begin{aligned} \sigma_x &= \sigma_h \\ \sigma_y &= \sigma_v \\ \tau_{xy} &= 0 \end{aligned} \tag{5.1}$$

So the stress solution will be reduced to the following form.

$$\sigma_r = \frac{\sigma_h + \sigma_v}{2}\left(1 - \frac{R_w^{\,2}}{r^2}\right) + \frac{\sigma_h - \sigma_v}{2}\left(1 + 3\frac{R_w^{\,4}}{r^4} - 4\frac{R_w^{\,2}}{r^2}\right)\cos(2\theta) + \frac{R_w^{\,2}}{r^2}\,p_w \tag{5.2}$$

$$\sigma_\theta = \frac{\sigma_h + \sigma_v}{2}\left(1 + \frac{R_w^{\,2}}{r^2}\right) - \frac{\sigma_h - \sigma_v}{2}\left(1 + 3\frac{R_w^{\,4}}{r^4}\right)\cos(2\theta) - \frac{R_w^{\,2}}{r^2}\,p_w \tag{5.3}$$

$$\tau_{r\theta} = -\frac{\sigma_h - \sigma_v}{2}\left(1 - 3\frac{R_w^{\,4}}{r^4} + 2\frac{R_w^{\,2}}{r^2}\right)\sin(2\theta) \tag{5.4}$$

where, r is the radial coordinate, θ is the tangential coordinate. The solution of the deformation are listed as well for verification.

$$\begin{aligned} u_r = {} & \frac{r}{4G}\left[\left(\sigma_h + \sigma_v\right)\left(\frac{\chi - 1}{2} + \frac{R_w^2}{r^2}\right)\right] + \\ & \frac{r}{4G}\left[\left(\sigma_h - \sigma_v\right)\left(\frac{R_w^2}{r^2}\left[\chi + 1 - \frac{R_w^2}{r^2}\right] + 1\right)\cos(2\theta) - 2\frac{R_w^2}{r^2}\,p_w\right] \end{aligned} \tag{5.5}$$

$$u_\theta = -\frac{r}{4G}\left(\sigma_h - \sigma_v\right)\left(\frac{R_w^2}{r^2}\left[\chi - 1 + \frac{R_w^2}{r^2}\right] + 1\right)\sin(2\theta) \tag{5.6}$$

where, G is shear modulus and χ is a material parameter which is equal to $3 - 4\nu$ for plane strain problems. The solution of displacement is the total displacement relative to the stress free intact rock derived for the dry rock condition. Since the analytical solution of displacement is derived for dry rock condition, total stress is used in the numerical study.

If the effective stress is used in the numerical study, the solution is the displacements of dry rock with effective stress exerted. The analytical solutions are simply (5.5) and (5.6) with stress replaced by the effective stress and wellbore pressure replaced by the differential wellbore pressure.

$$\begin{aligned} u_r = {} & \frac{r}{4G}\left[\left(\sigma_h + \sigma_v\right)\left(\frac{\chi - 1}{2} + \frac{R_w^2}{r^2}\right)\right] + \\ & \frac{r}{4G}\left[\left(\sigma_h - \sigma_v\right)\left(\frac{R_w^2}{r^2}\left[\chi + 1 - \frac{R_w^2}{r^2}\right] + 1\right)\cos(2\theta) - p_{pi}(\chi - 1) - 2\frac{R_w^2}{r^2}\,p_w\right] \end{aligned} \tag{5.7}$$

Furthermore, if the displacement caused by hydrostatic load is added then, total displacement for pressurized hole in drained rock can be obtained. The analytical solution for tangential displacement is the same as (5.6) while the radial displacement is expressed as:

$$u_r = \frac{r}{4G}\left[\left(\sigma_h+\sigma_v\right)\left(\frac{\chi-1}{2}+\frac{R_w^2}{r^2}\right)\right]+ \\ \frac{r}{4G}\left[\left(\sigma_h-\sigma_v\right)\left(\frac{R_w^2}{r^2}\left[\chi+1-\frac{R_w^2}{r^2}\right]+1\right)\cos(2\theta)\right]+r\left(\frac{1}{3K_s}-\frac{\chi-1}{4G}\right)p_{pi}-\frac{R_w^2}{2Gr^2}\,p_w \tag{5.8}$$

6.3 The comparison

Given the numerical code and the analytical solution, the results of the verification is presented below by investigating the displacement field.

In Figure 6-3, the displacement field in x-direction is plotted on the domain of original shape after applying the loads mentioned above calculated by NSMOOM.

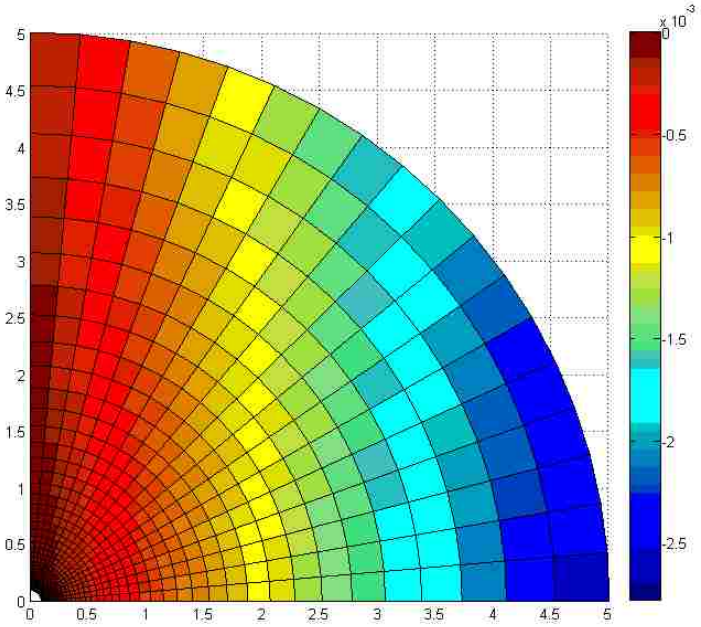

Figure 6-3 Displacement in x-direction by numerical simulation

The color represents the magnitude of the displacement scaled by the color bar to the right of the plot. The displacement at y-axis is zero because of the boundary condition. One can observe

that the displacements for the rest of the domain are all negative. Due to the sign convention, the whole domain moves to the left, i.e., the wellbore shrinks if no breakout happens yet, and the wellbore shrinks the most along the direction of minimum horizontal stress.

Similarly, the displacement field in y-direction is plotted as shown in Figure 6-4. Even though this plot looks like the previous one flipped with respect to $y = x$, the difference in the magnitude is obvious. The difference comes from the anisotropic boundary loading condition. The displacement in y-direction is larger than that in x-direction because the larger σ_y applied to the external boundary.

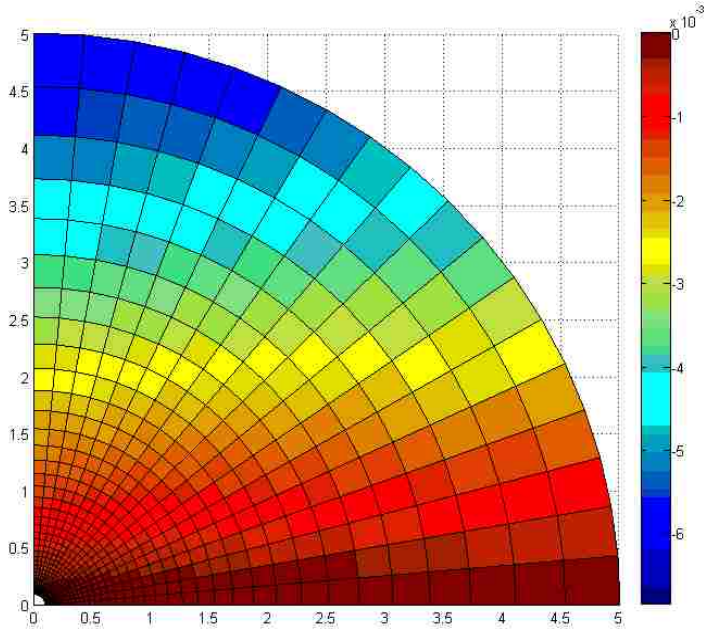

Figure 6-4 Displacement in y-direction by numerical simulation

Furthermore, a comparison between the numerical solution and the analytical solution is presented. Figure 6-5 (a) and (b) plots the numerical solution and the analytical solution of displacements of all nodes in x-direction and y-direction respectively.

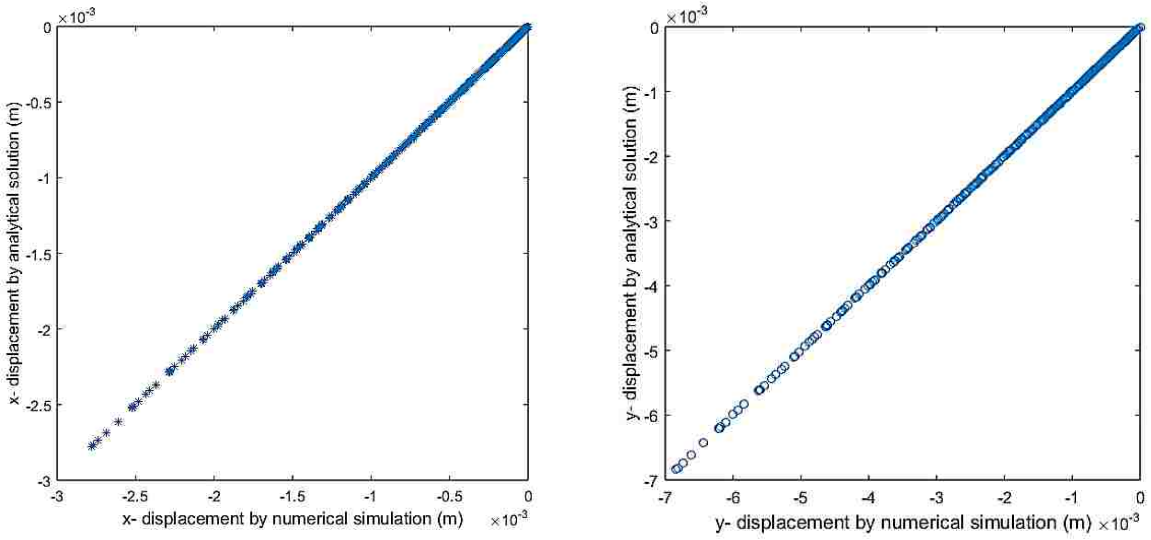

(a) (b)

Figure 6-5 Comparison of displacements between numerical and analytical method

Finally, the relative error is calculated to make a further confirmation.

$$Error = \frac{\sqrt{\sum_{i=1}^{n}\left(U_i - u_i\right)^2}}{\sqrt{\sum_{i=1}^{n} u_i^{\,2}}} \tag{5.9}$$

where, n is the total number of nodes, U_i and u_i is the numerical solution and the analytical solution of displacement of the i^{th} node respectively. For this specific verification case, the error for displacements in x-direction is 7.122×10^{-4} and that in y-direction is 4.763×10^{-4}, which are small enough to show the accuracy of NSMOOM for nodal displacements within the elastic domain. The verification of NSMOOM for plastic domain will be discussed in detail in the next chapter.

The strain and stress at the Gaussian integration points as functions of displacement gradient are directly recovered from the nodal displacements without considerable error. However, one should note that the comparison of stress and strain with analytical solution must look at the Gaussian integration points rather than the nodes if the comparison is required. This is determined

by the theory of finite element method. The recovered displacement gradients are most accurate on the integration points, whereas, considerable error can be introduced if the gradients are extrapolated to the nodes without special care. So the comparison of strain and stress on nodes are usually not satisfactory. One straightforward approach is to refine the mesh again and again so that the elements are small enough and the Gaussian integration points almost overlap the nodes. In addition, many special techniques have been proposed to improve the accuracy of recovered displacement gradients at node. The comparison can be referred to the work Hawken et al. in 1991 and one well-known method is called superconvergent recovery method (Hawken, Townsend, & Webster, 1991). Nevertheless, the procedure is rather lengthy and the stress and strain at the nodes are not necessary for the numerical simulation. As a result, NSMOOM doesn't extrapolate the recovered strain and stress to the nodes.

Chapter 7 The Application to an Under-balanced Drilling Case

This chapter simulated a real field case using the NSMOOM. The field data and the various model settings are discussed first. Then the same elastoplastic model is set up in a reputable commercial finite element analysis software, ABAQUS. A series of comparisons of the same elastoplastic model in the two simulators are elaborated for the verification of NSMOOM in the elastoplastic domain. The wellbore stability analysis of the field case is conducted via visualization of plastic yield zone and a concept of Normalized Yield Zone Area. Fortunately, some field observations pertaining wellbore stability issue are available for the studied field case. Therefore the prediction is compared to the actual field observation. Finally, the difference in predicting the wellbore stability by the proposed elastoplastic model and the linear elastic model is addressed. The difference further verifies the significance of using elastoplastic model to analyze wellbore stability.

7.1 Setup the numerical model in NSMOOM

Rock mechanical data from a real field drilling case are usually very limited. Fortunately, provided some detailed data for wellbore stability analysis. The oil field is located in the southern part of Iran representing a highly fractured limestone reservoirs with very low formation pore pressure gradients (Salehi et al., 2010). Underbalance drilling was dominant in that field because severe wellbore instability problems were very common during the overbalanced drilling due to the low pore pressure in the depleted fractured reservoir. However, the application of underbalanced drilling entails the risk of shear failure and wellbore collapse. This chapter is aimed at providing a good prediction of drilling mud density to avoid wellbore collapse by using the elastoplastic model. A horizontal well with $6.5 in$ wellbore diameter was drilled in this field at TVD of 8687 ft. Pore pressure gradient was reported as $5.56 lb/gal$ from DST test analysis. The

overburden stress was approximated from the bulk density. The magnitude of in-situ stress was also a function of pore pressure as reservoir was depleted. Assuming elastic response, a relationship between pore pressure and in-situ stress was found and used to predict the current in-situ stresses from the drop of pore pressure. The rock mechanical properties were determined from some laboratory tests while the initial cohesion was estimated from the assumption that the critical plastic strain is 0.05. Also the value for hardening modulus was an estimate. All the results are listed in the Table 7-1.

Table 7-1 Input parameters for wellbore stability analysis in the field

Parameters	Field	SI
Young's modulus, E	3.31×10^{6} *psi*	22821*MPa*
Poisson's ratio, ν	0.33	0.33
Friction angle, ϕ	41.5°	41.5°
Dilation angle, φ	41.5°	41.5°
Initial cohesion, c	1125 *psi*	7.76 *MPa*
Hardening modulus, H	14503.8 *psi*	100 *MPa*
Overburden stress, σ_v	−10424.40 *psi*	−71.87 *MPa*
Maximum horizontal stress, σ_H	−7036.47 *kpsi*	−48.51 *MPa*
Minimum horizontal stress, σ_h	−6254.64 *kpsi*	−43.12 *MPa*
Initial pore pressure, p_{pi}	2509.17 *psi*	17.30 *MPa*
Wellbore pressure, p_w	2346.71 *psi*	16.18 *MPa*
Wellbore radius, R_w	6.50 *in*	0.165 *m*
Reservoir radius, R_e	54.17 *ft*	16.5 *m*

The direction of minimum horizontal stress was obtained from oriented caliper logs of poor quality, which showed an approximate direction of N40W. Note that the directions of the wellbore axis and the horizontal stresses are critical to the analysis of wellbore stability. Due to the uncertainty, it is conservative to assume that the horizontal well would be drilled at the worst case for the wellbore stability where the wellbore is parallel to the direction of maximum horizontal stress in that the wellbore suffers the most severe deviatoric stress.

Underbalanced drilling means that the bottom-hole pressure should be less than the pore pressure. According to the field report, the equivalent circulating density is $5.20 lb/gal$, which is $0.36 lb/gal$ lower than the pore pressure. For the reservoir radius, the ratio R_e / R_w of 100 is usually large enough for the assumption of infinite reservoir.

The geometry setting of the domain is the similar as Figure 6-2, which is also a quarter-reservoir model due to the symmetry of the problem. More complicated calculations are involved in the elastoplastic model and a finer mesh method is adopted in the analysis comparing to the preliminary verification case. To make comparison with ABAQUS, the mesh generating method is exactly the same as that in ABAQUS by using single biased seeds. As Figure 7-1 shows, the whole domain are partitioned into two parts, so that the mesh can be refined in the near borehole part without increasing nodes number too much. The bias ratio is 15 for both parts. And the density for the two parts are $35*18$ and $15*18$ respectively. As a result, there are 900 elements and 969 nodes in the mesh profile which is almost the full capacity of the student edition of ABAQUS.

The elastoplastic simulation for actual wellbore drilling problem has two steps. First step sets the initial stress condition as in-situ effective stress. As for the boundary condition, all the four boundaries are fixed. These constraints are assured naturally in NSMOOM because all initial displacement are set to zero. Moving to the second step, the constraint of displacement along the

wellbore boundary is released. The boundary conditions along the two axes are changed back to symmetry condition as in the preliminary verification case. The loads exerted to the wellbore boundary is incrementally reduced to the differential wellbore pressure Δp_w. The simulation results will be illustrated in the next section along with the results by ABAQUS for comparison.

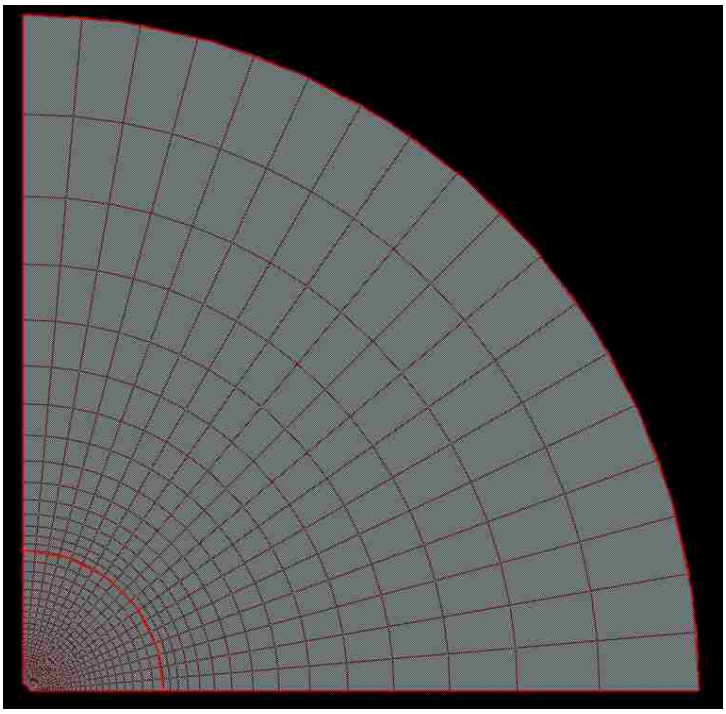

Figure 7-1 Refined mesh profile of the wellbore domain

7.2 The comparative deformation analysis with ABAQUS

A numerical model is set up in the student edition of ABAQUS with the same inputs. However, there are some differences in the model settings. According to the ABAQUS Analysis User's Guide, the yield condition of Drucker-Prager model is expressed as:

$$F = q + p\tan\beta - d = 0 \tag{5.10}$$

where, parameter q denotes the invariant of deviatoric stress, which can be related to J_2 by

$$q = \sqrt{3J_2} \tag{5.11}$$

Thus $\tan\beta$ and d can be retrieved from ξ and η after multiplying $\sqrt{3}$, that is

$$d = \sqrt{3}\xi c = \frac{3\sqrt{3}}{\sqrt{9+12\tan^2\phi}}c$$
$$\tan\beta = \frac{3\sqrt{3}\tan\phi}{\sqrt{9+12\tan^2\phi}} \tag{5.12}$$

Further note that ABAQUS does not have a block to input the hardening modulus. Instead, the hardening is first defined as pure shear type and the hardening parameter is cohesion d . Then the constant hardening modulus is represented by a series of data for cohesion and corresponding equivalent plastic strain forming a line with a constant slope.

The comparison between the two simulators considers the results after the final increment. Due to the difference in the internal algorithm of the two simulators, the comparative study pays more attention to the distribution than the absolute magnitude.

First, the displacements along the x-axis direction are visualized by contour plots in the near wellbore region as shown in Figure 7-2. From the right plot, one can easily see the size of near wellbore region. The color represents the magnitude of the displacements. The same sign convention which takes tension as positive is followed by both simulators.

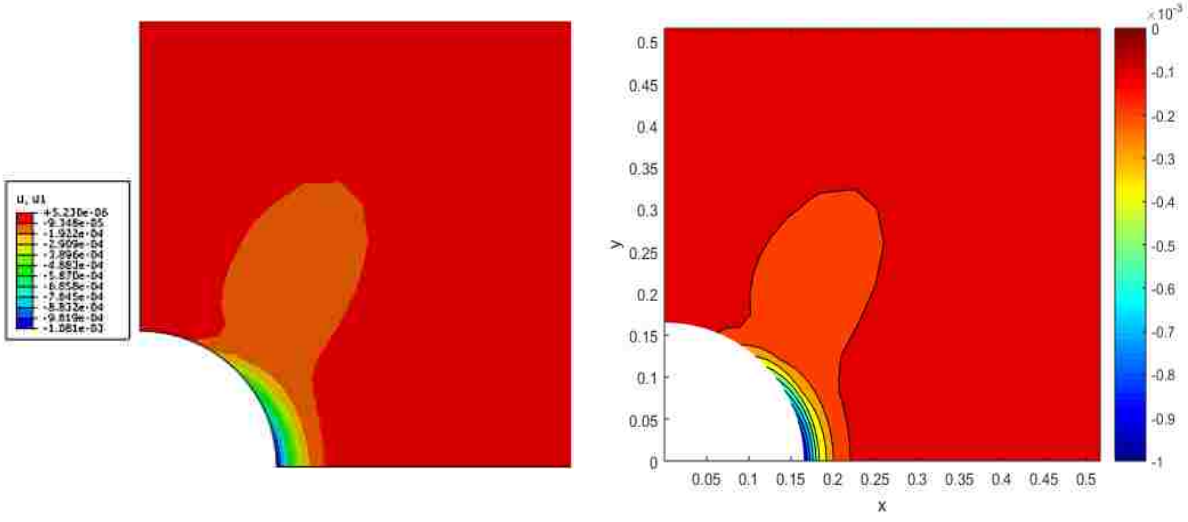

Figure 7-2 Comparison of displacements in x-axis direction. Left and right are generated by ABAQUS and NSMOOM respectively.

Similarly, the comparison for displacements in y-axis direction is shown in Figure 7-3. Similar distribution and similar range of the color bar can be observed.

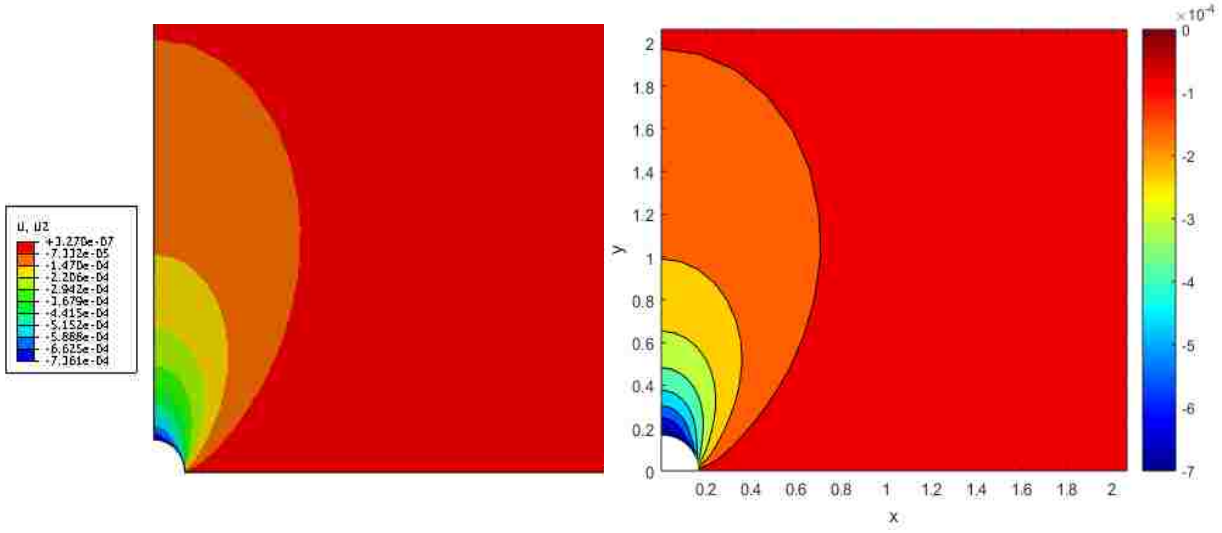

Figure 7-3 Comparison of displacements in y-axis direction. Left and right are generated by ABAQUS and NSMOOM respectively.

Later on, the displacements of nodes along certain path calculated by two simulators is plotted in the same figure. Here two paths are selected based on the geometric feature of the model. They are the wellbore boundary, and the path along 45^o radial direction.

In Figure 7-4 and Figure 7-5, the curves are plotted to show the displacements of nodes along the wellbore boundary path. The solid curve represents the results calculated by the NSMOOM while the other marked by the star sign is for the ABAQUS. One can observe that the trend of two curves in one figure are similar while two curves do not perfectly coincide. There can be a lot of causes for the gap since the comparison is between two independently programmed simulators, in other words, many internal setting can be different while the comparison should focus on the correctness of the implementation of Newton-Raphson algorithm and return-mapping method. After all, the gap is not that significant considering the order of magnitude of the unit. Furthermore the gap will be minimized as the strain and stress are recovered from the gradients of displacements

in that the distribution of the displacements for an element counts more than the absolute value of a single nodes.

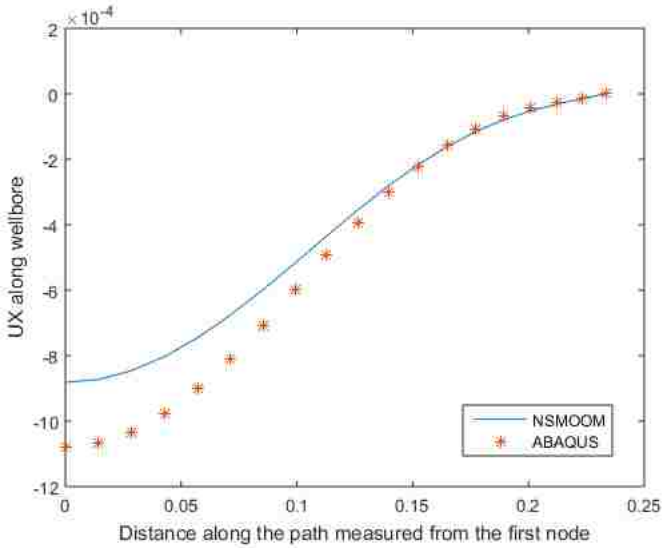

Figure 7-4 Comparison of displacements in x-axis direction of nodes along wellbore

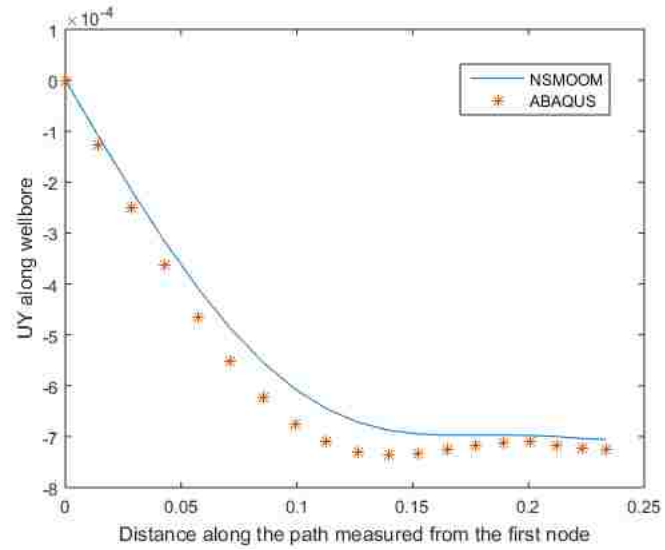

Figure 7-5 Comparison of displacements in y-axis direction of nodes along wellbore

Figure 7-6 and Figure 7-7 show good match of displacements between the two simulators for the region aside from the boundary, which means the developed simulator has implemented

the correct algorithm. The gap observed on the boundary comes from the issue of boundary settings. Overall, the comparison shows good results.

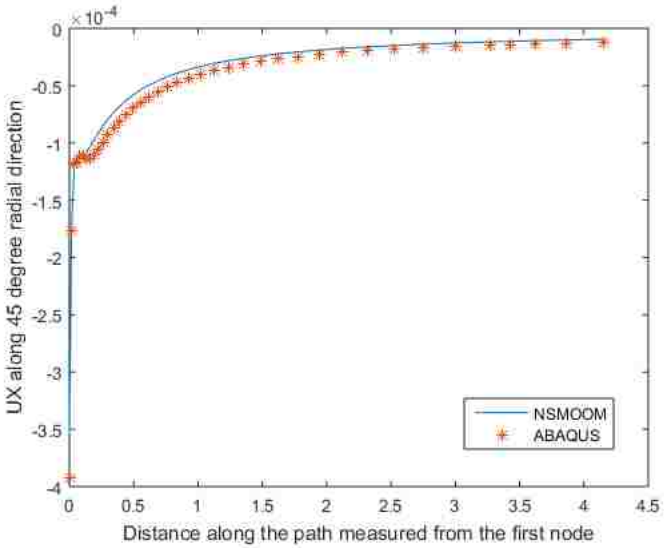

Figure 7-6 Comparison of displacements in x-axis direction of nodes along 45^{o} radial direction

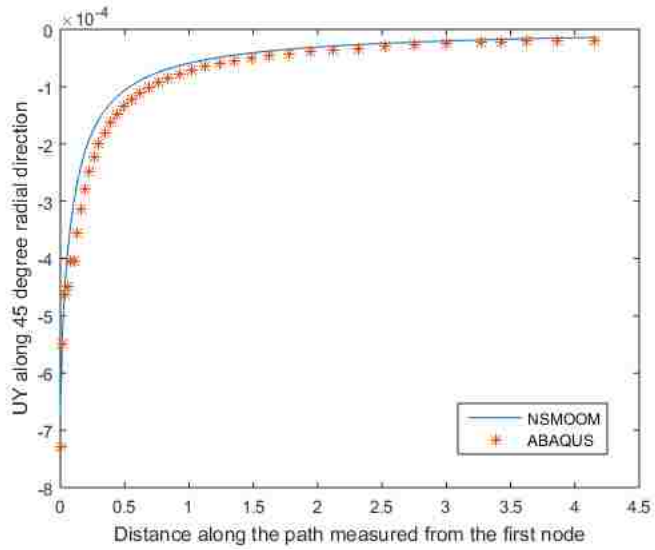

Figure 7-7 Comparison of displacements in y-axis direction of nodes along 45^{o} radial direction

Subsequently, the equivalent plastic strains $\bar{\varepsilon}^{p}$ calculated by the two simulators are compared. Since only a small portion adjacent to the wellbore yields at last, the contour plot can be seen in near wellbore region. As shown in Figure 7-8, one can observe a good match in the

prediction of the yield zone. The yielded zone was developed at the bottom of the wellbore region. If the wellbore would collapse, it would start from this yielded zone where the plastic strain is largest.

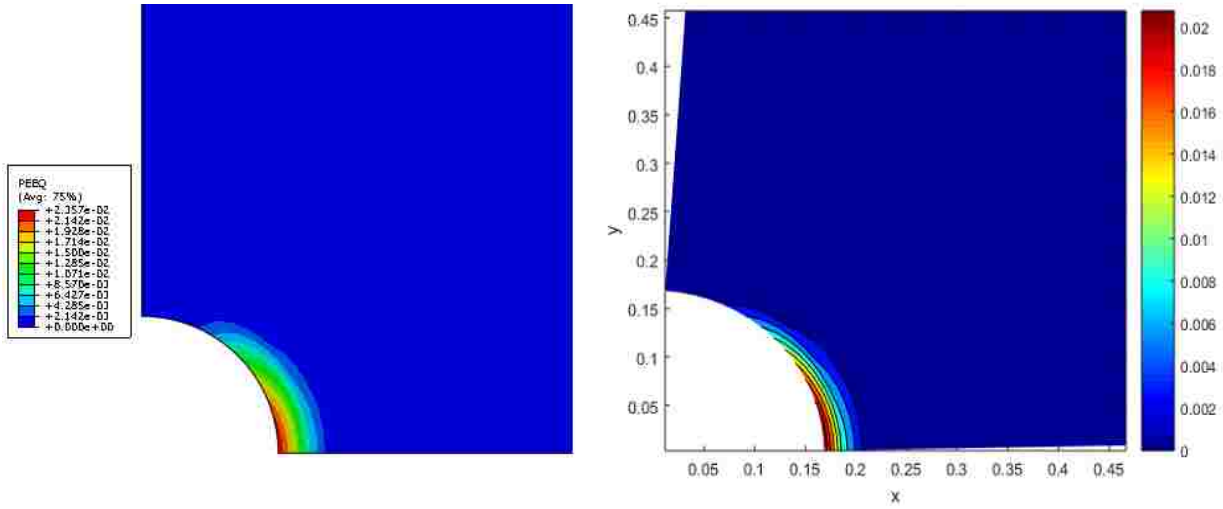

Figure 7-8 Comparison of equivalent plastic strain. Left and right are generated by ABAQUS and NSMOOM respectively.

Note that the values of strain and stress are calculated at the Gaussian integration points, NSMOOM doesn't extrapolate the values to the finite element nodes or to the continuous domain. That is why the right contour plot does not cover the whole near wellbore region. Whereas, ABAQUS does extrapolate the values at Gaussian points to continuous domain.

The magnitude comparison of equivalent plastic strain is shown in Figure 7-9. One can observe a perfect match of accumulated plastic strain between these two simulators even though the displacement calculation has a small gap. The accumulated plastic strain is computed by equation (4.23) directly during the return-mapping procedure with the plastic multiplier. In other words, the calculated plastic multiplier Λ has a good match with that by ABAQUS. The good match shown in the figure further verifies the correctness of NSMOOM with respect to the

implementation of Newton Raphson algorithm and the return-mapping method for Drucker-Prager model.

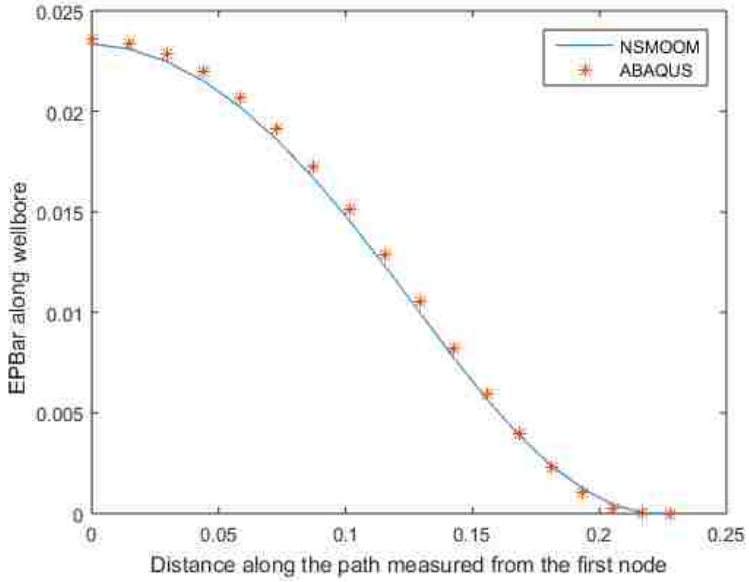

Figure 7-9 Accumulated plastic strain of elements along the wellbore

There are four components for a stress tensor for the plane strain problem. For the purpose of verification, only the two normal stresses within the plane are studied. In Figure 7-10, similar contour plots of normal stress in x-axis direction generated by the two simulator are displayed side by side.

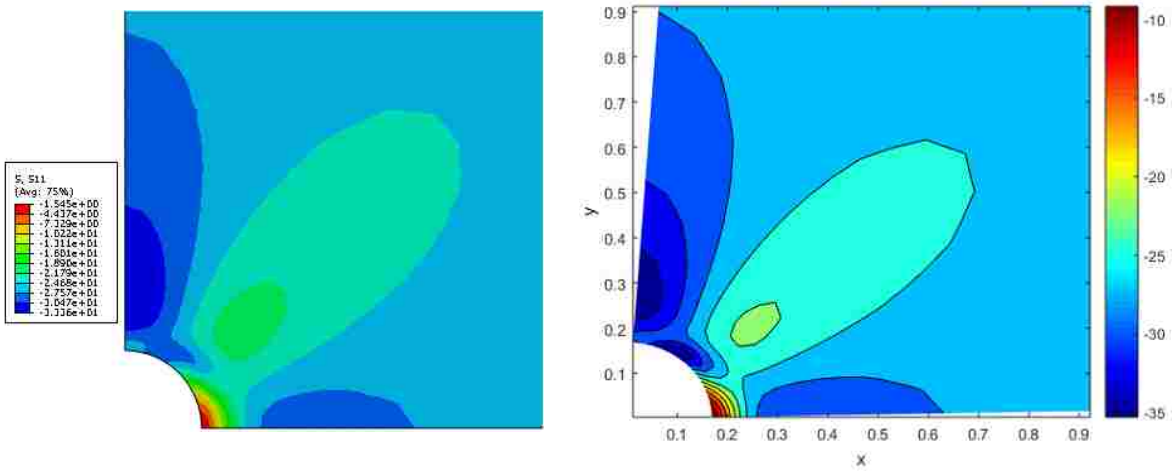

Figure 7-10 Comparison of normal stress in x-axis direction. Left and right are generated by ABAQUS and NSMOOM respectively.

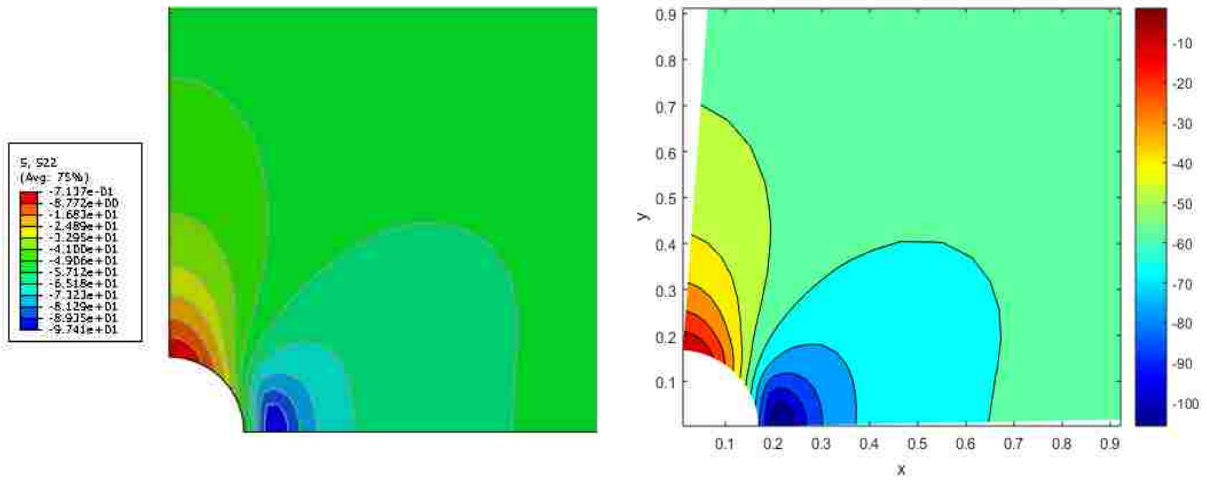

Figure 7-11 Comparison of normal stress in y-axis direction. Left and right are generated by ABAQUS and NSMOOM respectively.

In this section, the comparative deformation analysis is extensively presented by looking at the displacements, equivalent plastic strain and the stress. Preliminary observations are described as well. In conclusion, the results serve as a verification to the code and its implementation.

7.3 Wellbore stability analysis

As the material yields, the bonding forces between its grains weakens. In other words, the yielded zone becomes more susceptible to spalling due to the artificial effects, like pressure surges during trips and mechanical erosion by the drillstring (Hawkes & McLellan, 1996). Hawkes and Mclellan then proposed a criterion to assess the risk of wellbore instability based on the area of yielded zone (P. McLellan & Hawkes, 1999; P. J. McLellan & Hawkes, 1998; P. J. McLellan, Hawkes, & Read, 2000).

The Normalized Yielded Zone Area (NYZA) is defined to indicate the likelihood of borehole instability. NYZA is the cross-sectional area of the yielded rock around the borehole divided by the area of the original borehole. Several studies using this criterion have been reported in predicting wellbore instability problems and sand production problems. Experience shows that NYZA greater than 1.0 often indicates the onset of borehole complications, although this threshold

is subject to change due to the actual operating situation like well inclination, borehole cleaning capacity, etc. (Salehi et al., 2010).

$$\mathrm{NYZA} = \frac{A_{yield}}{A_{hole}} \tag{5.13}$$

The elastoplastic model provides an insight of the evolution of the yielded zone in the near wellbore region during the incremental loading. The evolution is displayed by a series of 2D surface plot of equivalent plastic strain $\bar{\varepsilon}^{p}$. In Figure 7-12, six plots are selected to show the development.

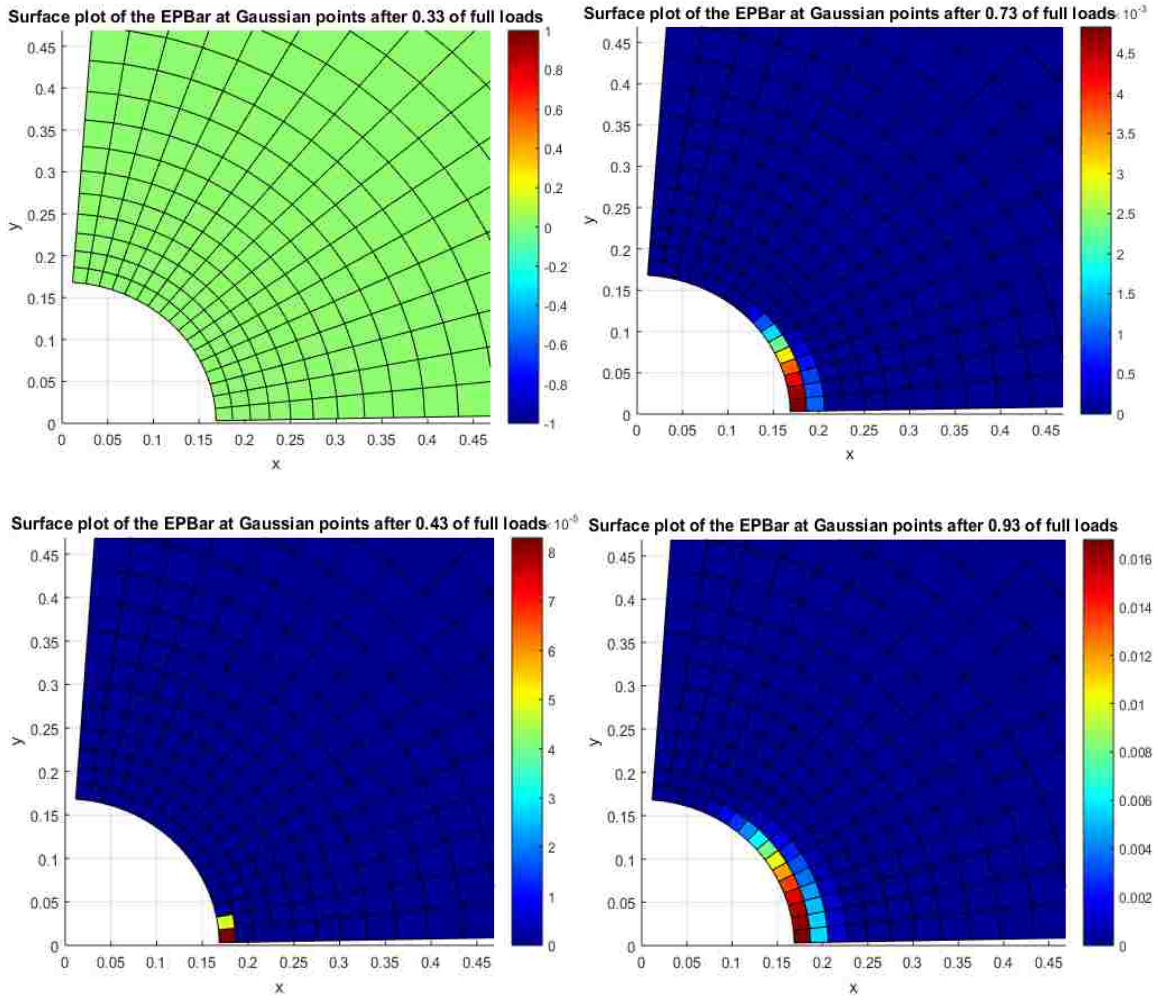

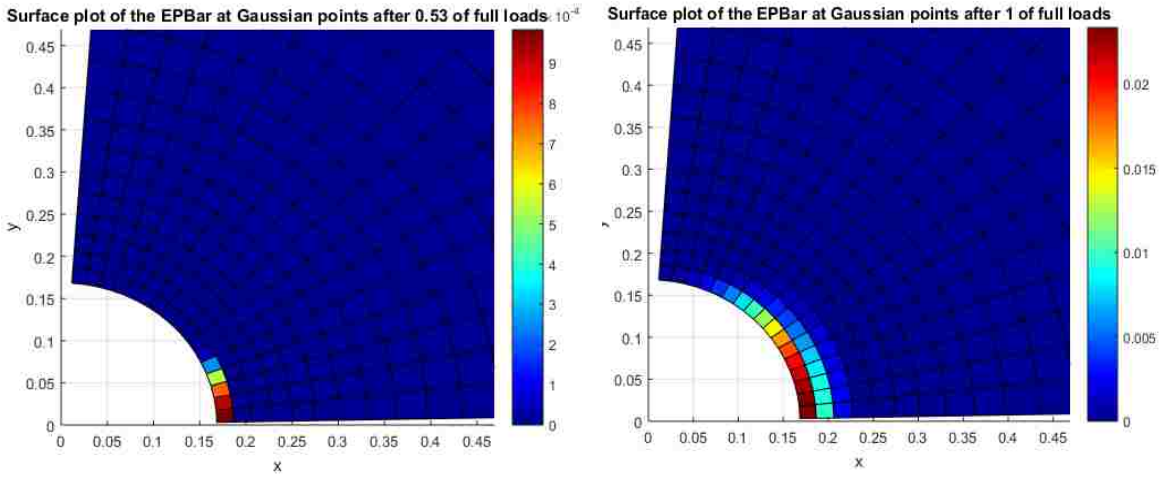

Figure 7-12 Evolution of plastic zone during incremental simulation

The first increment 33% of the total loads. The monochromatic map shows that the whole region is still pure elastic. The second plot at the increment of 43% is corresponding to the second point in Figure 7-13. As is shown, the plastic yielding starts from the intersection of borehole boundary and x-axis. As the incremental load increases, the yielded zone first expands upward then rightward.

In Figure 7-13, NYZA is plotted versus the value of increment to show the development.

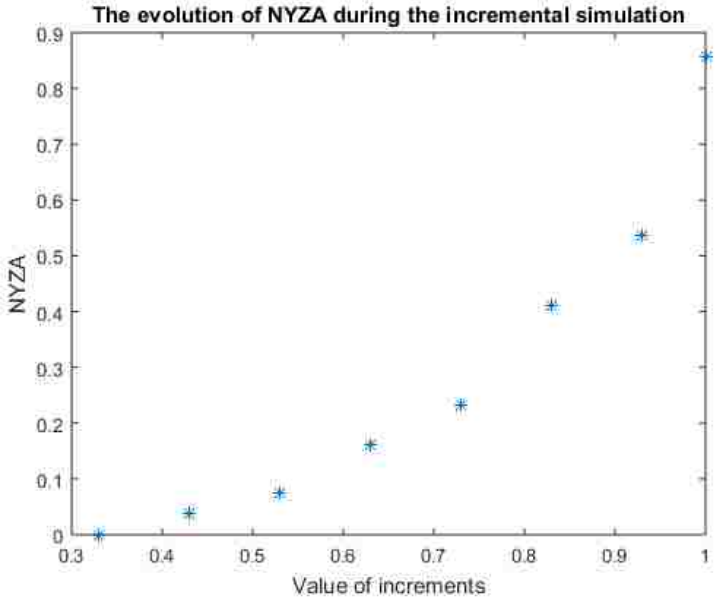

Figure 7-13 The evolution of NYZA during the incremental simulation

In the platform of elastoplastic model, NYZA keeps increasing as the loads is exerted incrementally. Clearly, the maximum value of NYZA is less than 1.0. Therefore, it is concluded that the wellbore keeps its integrity based on the proposed model and the data used for the analysis. According to the field observation, no severe borehole stability problem was reported although it is not safe to contend that the wellbore has not suffered any failure. Note that the rock has already failed amid the second and the third increment according to the pure elastic model.

The critical value of NYZA should be adjusted based on real situation or offset wells. For example, the value should be decreased if the rock formation is more susceptible to spalling because of natural fractures. Also it should be decreased accordingly if the wellbore profile is complex, like a horizontal wellbore where friction between drillstring and borehole surface is severe. Therefore, in this case study, it is better to set the critical value as 0.9. Further simulations shows that the ECD can be as low as $5.11 lb/gal$ before the NYZA exceeds 0.9. Also further simulations show that no available mud weight window can be provided for the under-balanced drilling from the linear elastic model with the Drucker-Prager failure criterion.

On one hand, the proposed model which allows wider mud weight window can eliminate the need for setting unnecessary intermediate casing strings. On the other hand, as shown in the case study, the proposed model can provide a feasible solution for a critical field condition where the conventional linear elastic model does not work. In conclusion, the proposed elastoplastic approach gives a more reliable prediction in this wellbore stability analysis.

Chapter 8 Conclusions, Discussions and Recommendations

8.1 Conclusions

1. A simulator named NSMOOM is programmed using the object-oriented MATLAB to solve to the constitutive models in rock mechanics. The linear elastic model and nonlinear strain-hardening Drucker-Prager model has been incorporated. The program is open to incorporate the other constitutive models with manageable effort.
2. The program is verified with an analytical solution in the elastic domain and with commercial software ABAQUS in the elastoplastic domain. The verifications show optimistic results. The correctness of nonlinear finite element algorithm for Drucker-Prager model is verified.
3. The numerical simulation of wellbore drilling problem is conducted using the proposed Drucker-Prager model. Both associative flow rule and non-associative flow rule are used. The simulation offers an approach to study the evolution of yielded zone in the near wellbore region.
4. The wellbore instability criterion of Normalized Yielded Zone Area is employed to predict the wellbore instability. In a case study, the prediction has a good match with the actual well response, and a lower boundary of the mud window is predicted.
5. The proposed elastoplastic method provides a more reliable prediction in wellbore stability compared to the pure elastic model. The elastoplastic model gives wider mud weight window, which will decrease the number of casing sections and thus, decreases the drilling and completion costs.

8.2 Discussions and recommendations

1. NSMOOM currently supports only two steps, the initial step and the loading step. In real engineering problem, multi-step problems also exist. The support for multi-step simulation is recommended for the extension.
2. The linear hardening rule makes the calculation easier and faster, however, the real hardening behavior, according to laboratory tests of rocks, is usually nonlinear. A stepwise linear hardening rule is recommended for further programming.
3. The proposed Drucker-Prager model considers strain hardening only. In addition, NSMOOM keeps the studied domain intact, i.e., no spalling in the near wellbore region is modeled during plastic yielding. Strain softening and spalling should be taken into account to better model the rock behavior in the damaging process.
4. Further work is recommended to study the quantitative relationship between the onset of instability problems and the critical value of NYZA by taking account for the live data in the field.
5. While the plane strain assumption is commonly used for the wellbore stability analysis, it is not naturally applicable for all wellbore conditions. 3D modeling is necessary for more complicated wellbore profiles.
6. Good performance of a numerical simulation relies on the good quality of data, including the in-situ stress and a series of rock mechanical data. However the data gathering is usually difficult for a real field. Further effort is recommended to retrieve field data more accurately and less costly.

Bibliography

Aadnoy, B. S., & Chenevert, M. E. (1987). Stability of Highly Inclined Boreholes (includes associated papers 18596 and 18736). doi:10.2118/16052-PA

Aadnoy, B. S., & hogskole, N. t. (1987). *Continuum Mechanics Analysis of the Stability of Inclined Boreholes in Anisotropic Rock Formations*: Norwegian Institute of Technology.

Al-Ajmi, A. M., & Zimmerman, R. W. (2009). A new well path optimization model for increased mechanical borehole stability. *Journal of Petroleum Science and Engineering, 69*(1–2), 53-62.

Borja, R. I., Sama, K. M., & Sanz, P. F. (2003). On the numerical integration of three-invariant elastoplastic constitutive models. *Computer Methods in Applied Mechanics and Engineering, 192*(9), 1227-1258.

Bradley, W. B. (1979). Failure of Inclined Boreholes. *Journal of Energy Resources Technology-Transactions of the Asme, 101*(4), 232-239. Retrieved from <Go to ISI>://WOS:A1979HY67500004

Bradley, W. B. (1979). Mathematical concept-Stress Cloud-can predict borehole failure. *Oil Gas J.;(United States), 77*(8).

Chen, W. F., & Mizuno, E. (1990). *Nonlinear analysis in soil mechanics*. Amsterdam: Elsevier.

David, M. P. (1999). *Finite element analysis in geotechnical engineering*: Thomas Telford Publishing.

de Souza Neto, E. A., Perić, D., & Owen, D. R. J. (2008). Computational Methods for Plasticity: Theory and Applications *Computational Methods for Plasticity*: John Wiley & Sons, Ltd.

Dubois-Pèlerin, Y., Zimmermann, T., & Bomme, P. (1992). Object-oriented finite element programming: II. A prototype program in Smalltalk. *Computer Methods in Applied Mechanics and Engineering, 98*(3), 361-397.

Fung, L. S. K., Wan, R. G., Rodriguez, H., Silva Bellorin, R., & Zerpa, L. (1999). An Advanced Elasto-plastic Model For Borehole Stability Analysis of Horizontal Wells In Unconsolidated Formation. doi:10.2118/99-12-01

Haimson, B. (2006). Micromechanisms of borehole instability leading to breakouts in rocks. *International Journal of Rock Mechanics and Mining Sciences, 44*(2), 157-173. doi:http://dx.doi.org/10.1016/j.ijrmms.2006.06.002

Hawken, D., Townsend, P., & Webster, M. (1991). A comparison of gradient recovery methods in finite - element calculations. *Communications in Applied Numerical Methods, 7*(3), 195-204.

Hawkes, C. D., & McLellan, P. J. (1996). *Modeling of Yielded Zone Enlargement Around a Wellbore*.

Hsiao, C. (1988). A Study of Horizontal-Wellbore Failure. doi:10.2118/16927-PA

Kang, Y., Yu, M., Miska, S. Z., & Takach, N. (2009). *Wellbore Stability: A Critical Review and Introduction to DEM*.

Ledgerwood. (1988). AN INVESTIGATION OF THE EFFECTS OF DEFORMATION-INDUCED PORE PRESSURE ON THE FAILURE OF ROCK. *Hughes Tool Company*.

Mackie, R. I. (1992). Object oriented programming of the finite element mehtod. *International Journal for Numerical Methods in Engineering, 35*.

Mackie, R. I. (2001). *Object oriented methods and finite element analysis*: Kippen, Stirling : Saxe-Coburg Publications, 2001.

McLean, M. R., & Addis, M. A. (1990). *Wellbore Stability Analysis: A Review of Current Methods of Analysis and Their Field Application*.

McLellan, P., & Hawkes, C. (1999). *Borehole Stability Analysis For Underbalanced Drilling*.

McLellan, P. J., & Hawkes, C. D. (1998). *Application of Probabilistic Techniques for Assessing Sand Production and Borehole Instability Risks*.

McLellan, P. J., Hawkes, C. D., & Read, R. S. (2000). *Sand Production Prediction for Horizontal Wells in Gas Storage Reservoirs*.

Morita, N., & Gray, K. E. (1980). *A Constitutive Equation For Nonlinear Stress-Strain Curves In Rocks And Its Application To Stress Analysis Around A Borehole During Drilling*.

Papanastasiou, P., Thiercelin, M., Cook, J., & Durban, D. (1994). *Behaviour and Stability Analysis of a Wellbore Embedded in an Elastoplastic Medium*.

Paulino, E. N. L. G. H. (1999). Nonlinear Finite Element Analysis using an Object-Oriented Philosophy – Application to Beam Elements and to the Cosserat Continuum. *Engineering with Computers, 15*, 73-89.

Rockafellar, R. T. (1970). *Convex analysis*: Princeton university press.

Rockafellar, R. T., & Wets, R. J.-B. (2009). *Variational analysis* (Vol. 317): Springer Science & Business Media.

Salehi, S., Hareland, G., & Nygaard, R. (2010). Numerical simulations of wellbore stability in under-balanced-drilling wells. *Journal of Petroleum Science and Engineering, 72*(3–4), 229-235. doi:http://dx.doi.org/10.1016/j.petrol.2010.03.022

Sandler, I. S. (2005). Review of the development of cap models for geomaterials. *Shock and Vibration, 12*(1), 67-71.

Santarelli, F. J. (1987). *Theoretical and experimental investigation of the stability of the axisymmetric wellbore.* (Ph.D.), University of London.

Simo, J. C., & Hughes, T. J. R. (1998). *Computational Inelasticity* (Vol. 7). New York: Springer.

Spiezia, N., Salomoni, V. A., & Majorana, C. E. (2015). Plasticity and strain localization around a horizontal wellbore drilled through a porous rock formation. *International Journal of Plasticity, 78*, 114-144. doi:http://dx.doi.org/10.1016/j.ijplas.2015.10.013

Veeken, C. A. M., Walters, J. V., Kenter, C. J., & Davies, D. R. (1989). *Use of Plasticity Models For Predicting Borehole Stability*.

Westergaard, & Malcolm, H. (1940). Plastic state of stress around a deep well. *Journal of the Boston Society Civil Engineers, 27*(1), 1-5.

Zervos, A., Papanastasiou, P., & Cook, J. (1998). *Elastoplastic Finite Element Analysis of Inclined Wellbores*.

Zervos, A., Papanastasiou, P., & Vardoulakis, I. (2001). Modelling of localisation and scale effect in thick-walled cylinders with gradient elastoplasticity. *International Journal of Solids and Structures, 38*(30–31), 5081-5095. doi:http://dx.doi.org/10.1016/S0020-7683(00)00337-1

Zhang, K., Hopperstad, O. S., Holmedal, B., & Dumoulin, S. (2014). A robust and efficient substepping scheme for the explicit numerical integration of a rate-dependent crystal plasticity model. *International Journal for Numerical Methods in Engineering, 99*(4), 239-262. doi:10.1002/nme.4671

Zhou, S., Hillis, R., & Sandiford, M. (1996). On the Mechanical Stability of lnclined Wellbores. doi:10.2118/28176-PA

Zienkiewicz, O., Norris, V., Winnicki, L., Naylor, D., & Lewis, R. (1978). A unified approach to the soil mechanics problems of offshore foundations. *In: Numerical methods in offshore engineering.*

Zimmermann, T., Dubois-Pèlerin, Y., & Bomme, P. (1992). Object-oriented finite element programming: I. Governing principles. *Computer Methods in Applied Mechanics and Engineering, 98*(2), 291-303. doi:http://dx.doi.org/10.1016/0045-7825(92)90180-R

Vita

Chang Huang is an international student from Henan Province, China. Chang holds his B.E. degree in petroleum engineering from China University of Petroleum (East China). During his bachelor study, he was sponsored by the China Scholarship Council to do research at the University of New South Wales in Australia. He began his study at Louisiana State University in August of 2014. Chang worked as a teaching assistant for well design-drilling course Professor Andrew Wojtanowicz. Then he started his research project with Professor Babak Akbari. In 2015, Chang was awarded the Drilling Engineering Graduate Assistantship by the American Association of Drilling Engineers—New Orleans Chapter.